

# *eROSITA* study of the 47 Tucanae globular cluster<sup>★</sup>

Sara Saeedi<sup>1</sup>, Teng Liu<sup>2</sup>, Jonathan Knies<sup>1</sup>, Manami Sasaki<sup>1</sup>, Werner Becker<sup>2</sup>, Esra Bulbul<sup>2</sup>, Konrad Dennerl<sup>2</sup>, Michael Freyberg<sup>2</sup>, Roman Laktionov<sup>1</sup>, and Andrea Merloni<sup>2</sup>

<sup>1</sup> Dr. Karl Remeis-Sternwarte, Erlangen Centre for Astroparticle Physics, Friedrich-Alexander-Universität Erlangen-Nürnberg, Sternwartstrasse 7, 96049, Bamberg, Germany  
e-mail: sara.saeedi@fau.de

<sup>2</sup> Max-Planck-Institut für extraterrestrische Physik, Giessenbachstraße 1, 85748 Garching bei München, Germany

Received DATE; accepted DATE

## ABSTRACT

**Aims.** We present the results of the analysis of five observations of the globular cluster 47 Tucanae (47 Tuc) with *eROSITA* (extended Roentgen Survey with an Imaging Telescope Array) on board Spektrum-Roentgen-Gamma (Spektr-RG, SRG). The aim of the work is the study of the X-ray population in the field of one of the most massive globular clusters in our Milky Way. We focused on the classification of point-like sources in the field of 47 Tuc. The unresolved dense core of 47 Tuc (1'.7 radius) and also the sources, which show extended emission are excluded in this study.

**Methods.** We applied different methods of X-ray spectral and timing analysis together with multi wavelength studies for the classification of the X-rays sources in the field of 47 Tuc.

**Results.** We detected 888 point-like sources in the energy range of 0.2–5.0 keV. We identified 126 background AGNs and 25 foreground stars. One of the foreground stars is classified as a variable M dwarf. We also classified 14 X-ray sources as members of 47 Tuc, including 1 symbiotic stars, 2 quiescent low mass X-ray binaries, and 4 cataclysmic variable. There are also 5 X-ray sources, which can either be a cataclysmic variable or a contact binary, and also 1 X-ray sources which can be an active binary (Type RS CVn). We identified one X-ray binary, which belongs to the Small Magellanic Cloud. Moreover, we calculated the X-ray luminosity function of 47 Tuc. No significant population that seems to belong to the globular cluster has been observed in the energy range of 0.5–2.0 keV using *eROSITA* observations.

**Key words.** Galaxy: globular cluster, X-rays: binaries, stars: binaries: symbiotics, stars: binaries: cataclysmic variables

## 1. Introduction

Globular clusters (GCs) are known as spherical shaped, compact, old, and bright accumulations of stars, which are mainly observed in the halo, thick disk, and the bulge of the Galaxy, while they are not present in the thin disk (e.g. Gratton et al. 2019). The dynamical structure of the GCs is ideal for the formation of a large number of binary systems, especially short-period close binaries. Several studies (e.g. Gendre et al. 2003; Pooley et al. 2003; Heinke et al. 2003) have shown that there is a significant correlation between the number of low luminosity X-ray sources in GCs and the encounter frequency in GCs rather than with the mass of GCs. This means that X-ray sources with  $L_x > 10^{31} \text{ erg s}^{-1}$  in dense clusters are to a large extent dynamically formed. As the X-ray studies show the lower-density globular clusters are more dominated by BY Dra and RS CVn systems (e.g. Bassa et al. 2004, 2008; Cheng et al. 2018; Belloni et al. 2019; Heinke et al. 2020). So far, various types of X-ray binary systems have been frequently observed in GCs. The observation of the bright persistent low mass X-ray binaries (LMXBs;  $L_x > 10^{35} \text{ erg s}^{-1}$ ) in GCs started since the earliest X-ray missions (e.g. Uhuru, Cominsky et al. 1977). Since then it was suggested that the mass-normalized formation rate of LMXBs in GCs is orders of magnitudes higher than in the Galactic disk due to the high stellar densities in the core of the GCs (Clark 1975). Later studies confirmed the presence of eight persistently luminous

LMXBs in the GCs (Bahramian et al. 2014) and additional transient LMXBs have been detected in outbursts (e.g. Altamirano et al. 2008; Heinke et al. 2010; Sanna et al. 2017, 2018; Homan et al. 2018). The main population of X-ray sources in the GCs is that of the less luminous X-ray sources ( $L_x \lesssim 10^{33} \text{ erg s}^{-1}$ ), which are potentially a mixture of quiescent LMXBs, different types of accreting white dwarfs (AWDs), radio millisecond pulsars (MSP), and magnetically active binary systems.

In this work, we study the population of X-ray sources in the field of the Galactic globular cluster 47 Tucanae (47 Tuc) observed with *eROSITA*. 47 Tuc (also known as NGC 104; RA: 00h24m05.36s, DEC:  $-72^\circ 04' 53.2''$ ) with a half mass radius of 2'.76 and a mass of  $7.10 \times 10^5 M_\odot$  is one of the most massive GC in the Galaxy (Marks & Kroupa 2010). Hansen et al. (2013) measured an age of  $9.7 \pm 0.4$  Gyr and a metallicity of  $[\text{Fe}/\text{H}] = -0.75$  for 47 Tuc. The most updated distance measurement using parallaxes from Gaia (2nd data release) yields a distance of  $4.45 \pm 0.01 \pm 0.12$  for 47 Tuc (Chen et al. 2018). The first identification of the X-ray sources in the core of 47 Tuc has been performed using the data of *EINSTEIN* (e.g. Hertz & Grindlay 1983; Paresce et al. 1992; Auriere et al. 1989) and *ROSAT*, observatories (Hasinger et al. 1994; Verbunt & Hasinger 1998). Later studies using the high resolution cameras of *Chandra* identified more than one hundred X-ray sources in the core of 47 Tuc, including fifteen X-ray counterparts of the known radio millisecond pulsar at that time (Grindlay et al. 2001). Edmonds et al. (2003) performed the first deep optical/X-ray study using the

<sup>★</sup> Based on observations obtained with *eROSITA*.

data of *Chandra* and *Hubble Space Telescope*. In their study, optical counterparts of cataclysmic variables and active binaries have been found. Using deeper data of *Chandra*, Heinke et al. (2005) published a catalogue of three hundred X-ray sources within the half-mass radius and presented a classification of different types of X-ray sources. Bhattacharya et al. (2017) studied the sources of the core of 47 Tuc within a radius of  $2'.7$  using *Chandra* observations and performed X-ray spectral analysis for known MSPs identified in a radio survey (Ridolfi et al. 2016). They also reported the classification of five active binary systems in 47 Tuc. Moreover, recently, Cheng et al. (2019) studied the distribution of both faint and bright X-ray sources within the radius of  $7'.5$ . (see Fig. 1). For the first time, *eROSITA* has provided X-ray data of the field around 47 Tuc with in a large area of  $40'$  radius, which enables us to perform the analysis of the X-ray sources of 47 Tuc in a noticeably larger region than in *Chandra* studies as mentioned above. However, we had to ignore the central  $1'.7$  circular region of 47 Tuc in the *eROSITA* data since the emission is spatially unresolved. This paper reports the details of the X-ray analysis along with multi-wavelength studies (mainly in optical, infrared and near infrared), aiming at the classification of X-ray sources in the field of 47 Tuc. In Section 2, we describe the data reduction, source detection, and the source catalogue preparation. In Sections 4 and 3, we present the multi-wavelength studies and the X-ray analysis, respectively, which are used to classify the X-ray sources. In Section 5, we discuss the details of the classification of detected sources in the field of 47 Tuc.

## 2. *eROSITA* data analysis

### 2.1. Data reduction and source detection

We have analysed 5 observations of *eROSITA* taken in the Calibration and Performance Verification (CalPV, Predehl et al. 2021) phase in 2019. The details of the observations, which are sorted by date are shown in Table 1. Data reduction and source detection were performed using the *eROSITA* Science Analysis Software System eSASSusers\_201009 (Brunner et al., 2021, A&A, submitted).

In this work, the source detection was run only on single observations and in each observation the data of all 7 telescope modules (TMs) of *eROSITA* have been used in this work (Predehl et al. 2021). The light curve of the event files have been used to filter the possible soft proton flares of the observations by a threshold of  $30 \text{ cts s}^{-1} \text{ deg}^{-2}$ . Table 1 shows the sum of good time intervals for each observation. The detection process has been run over the event files of the observations in four energy bands of 0.2–0.6 keV, 0.6–1.1 keV, 1.1–2.3 keV, and 2.3–5.0 keV, where the fourth band is considered as the hard band of *eROSITA* (e.g. Brunner et al. 2021). Since the effective area of *eROSITA* noticeably decreases above 2.3 keV (Merloni et al. 2012), the majority of the sources can not be detected significantly above 2.3 keV. We selected a minimum maximum likelihood ( $L$ ) of 10 for the source detection (ermldet task in eSASS), which is equivalent to  $> 4\sigma$  significance according to the probability of Poisson random fluctuations of the counts ( $p$ ) detection minimum likelihood  $L = -\ln(p)$ . In this work, we study the point-like sources with an extent likelihood of 0 and exclude all the extended sources, which are probable candidates for, e.g., galaxy clusters, diffuse emission, bubble-like structures, etc. and will be studied in more details in future publications. Figure 1 shows the mosaic image of five observations of *eROSITA* of the field of 47 Tuc. With *eROSITA*, one bright source is detected at the

Table 1: *eROSITA* observations of 47 Tuc

OBS-N0	OBS-ID	OBS-Date	EXP.T* (ks)
1	700012	2019-09-28	19.5
2	700011	2019-11-01	25.8
3	700163	2019-11-02	25.3
4	700013	2019-11-02	25.2
5	700014	2019-11-02	25.2

\*:Net exposure time of observations.

Table 2: Offsets of the *eROSITA* observations

OBS-N0	$\Delta\text{RA}$ (")	$\Delta\text{DEC}$ (")
OBS1	$12.6^{+1.27}_{-1.34}$	$1.44^{+0.49}_{-0.40}$
OBS2	$7.0^{+1.44}_{-1.15}$	$2.91^{+0.47}_{-0.47}$
OBS3	$11.72^{+0.30}_{-0.34}$	$0.65^{+0.15}_{-0.10}$
OBS4	$11.47^{+1.27}_{-1.29}$	$4.02^{+0.44}_{-0.30}$
OBS5	$7.21^{+0.92}_{-1.06}$	$0.84^{+0.50}_{-0.50}$

The astrometric correction from Liu et al., (in prep.)

position of the centre of 47 Tuc, which was resolved into multiple sources with *Chandra* (Grindlay et al. 2001). This area was excluded in this study.

### 2.2. Astrometric correction

The astrometric corrections of the 47 Tuc observations were calculated by Liu et al. (in prep.) in two steps. First, sources were detected in each observation and the relative correction of the coordinates with respect to OBS3 was calculated for the other observations. To calculate the corrections, only bright point sources with detection likelihood  $> 12$  within an off-axis angle of  $25'$  were used, thus excluding sources with poor positional uncertainties. The uncertainties of the required corrections were calculated through bootstrapping. It was found that a coordinate shift ( $\Delta\text{RA}$ ,  $\Delta\text{DEC}$ ) is sufficient and a rotation correction is not needed. The events of all the observations were corrected for the relative astrometry and merged afterwards. In the second step, the source catalogue from the merged data was matched to the CatWISE 2020 catalogue (Marocco et al. 2021). Based on the highly reliable positions of the CatWISE counterparts of the X-ray sources, a second-pass correction was calculated. The total corrections applied to each of the 47 Tuc observations are listed in Table 2. We applied the same corrections to our catalogue.

### 2.3. Source Catalogue

The final catalogue of point-like sources in the field of 47 Tuc is obtained by cross-checking all detected sources between the five observations. If sources, which have been detected in at least two observations, were closer to each other than the  $3\sigma$  positional errors, they are considered as the same source. Sources, which were detected only in one of the observations near gaps or edges of the CCD chips or could be recognised as hot pixels, were removed from the source list. Table B.1 presents the final list of 888 X-ray sources in the field of 47 Tuc. The catalogue lists source ID, RA, Dec, positional uncertainty, flux of the source in different observations, hardness ratio, variability factor, and the class if a source was classified. The ID of the sources in Table B.1 is used to present the source in this work.

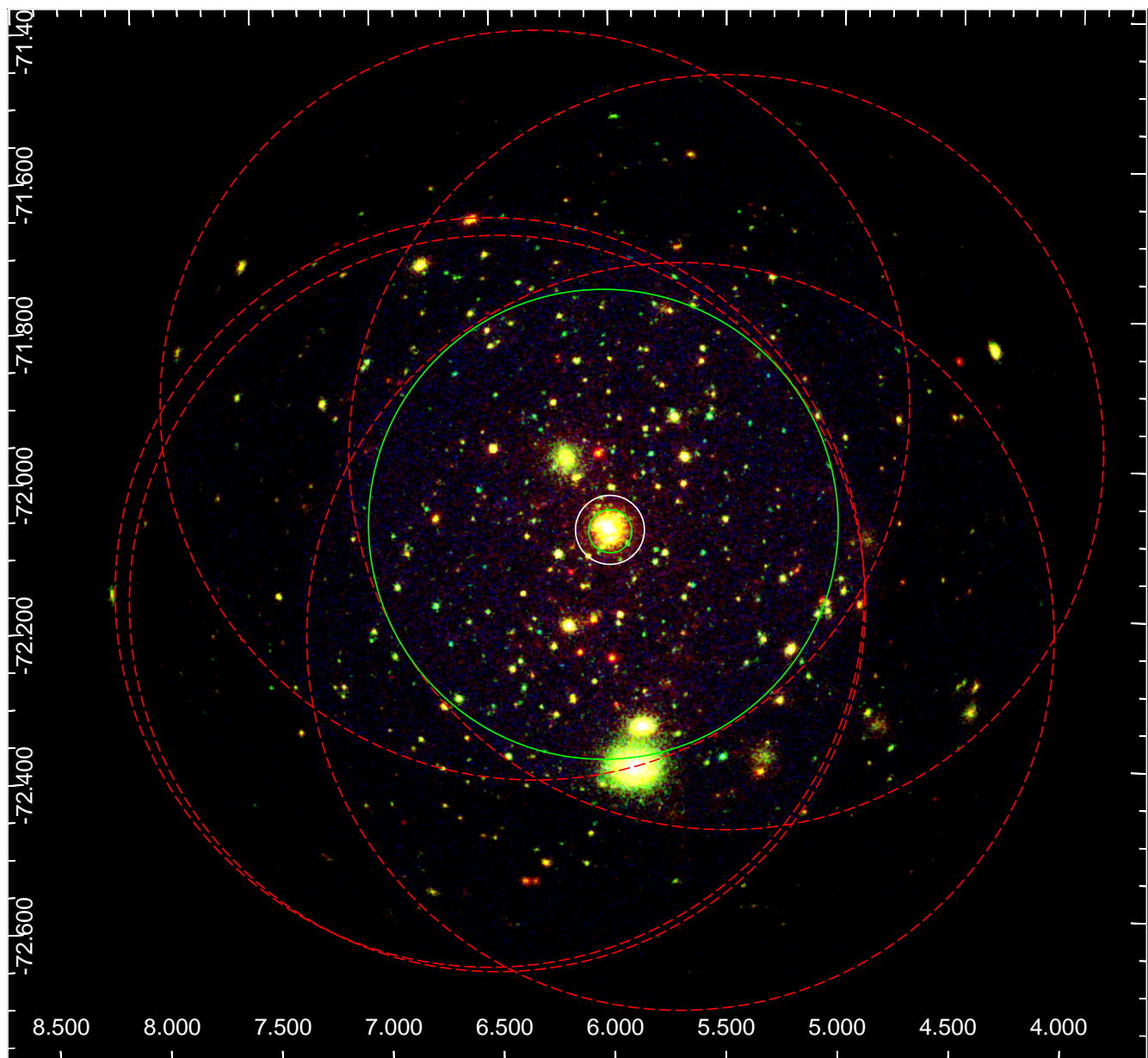


Fig. 1: Combined X-ray image of *eROSITA* observations in the field of 47 Tuc with a total radius of 42'. In this work all the visible point-like sources (888 sources) are studied. The half-mass radius of 47 Tuc is shown within the hard white region. The dashed red circles show the regions observed by five *eROSITA* observations. The larger and smaller hard green regions with radii of 18'.8 and 1'.7, show the area, which is covered by all observations and the extent of the unresolved emission from the center of 47 Tuc, respectively. The area between these two regions have been used to calculate the X-ray luminosity function (see Sect. 5.5).

### 3. X-ray analysis

To extract the light curves and the spectra of the sources we used `eSASS/srctool-V.1.61`; (Brunner et al., 2021, A&A, submitted).

#### 3.1. X-ray timing analysis

We carried out X-ray timing analysis for both short-term variability (periodicity and pulsation studies) and long-term variability. For all unknown sources with counts > 100, which have not been confirmed as foreground stars or AGNs in available catalogues, we searched for pulsation signals using the pulsation  $Z_n^2$  test (Buccheri et al. 1983, 1988). For unknown sources with

counts > 300 in each observation, we extracted the light curves of five observations and applied the Lomb-Scargle technique (Scargle 1982) to find a signal of pulsation and or periodicity. We could not find any significant pulsation or periodicity in the X-ray data of bright sources, which are candidates of neither foreground star nor background AGN.

To study the long term variability, we checked the flux variation of sources over five observations. Flux variation and its significance were calculated using

$$Var = \frac{F_{\max}}{F_{\min}} \text{ and } S = \frac{F_{\max} - F_{\min}}{\sqrt{EF_{\max}^2 + EF_{\min}^2}}, \quad (1)$$

respectively (Primini et al. 1993). Here,  $F_{\max}$  and  $F_{\min}$  are the maximum and minimum X-ray flux, and  $EF_{\min}$  and  $EF_{\max}$  are



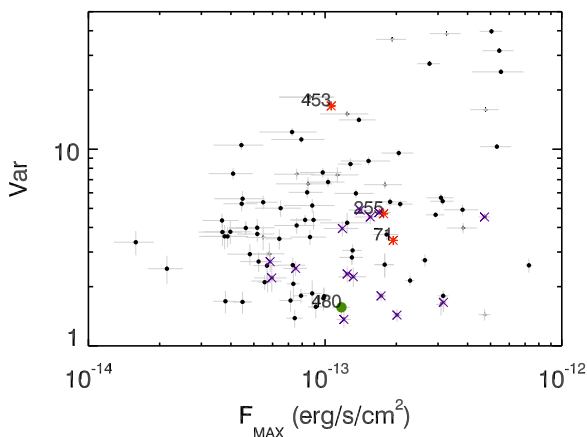


Fig. 2: Variability factor of sources with significant variability ( $S > 3$ ) in the energy band of 0.2–5.0 keV plotted versus the maximum flux. The symbols characterise foreground stars (\*), background objects ( $\times$ ), sources with counterpart classified as RGBs in 47 Tuc ( $\bullet$ ), main sequence member of 47 Tuc ( $\bullet$ ), members of SMC ( $\bullet$ ), and unclassified sources ( $\bullet$ ).

their corresponding errors. For all source, which have been detected in both observations the variability factor was calculated (see Table B.1). Sources with  $S > 3$  are considered as sources with significant variability. Figure 2 shows the significant variable sources versus the maximum flux of the source. As one can see the nature of the most variable source in the field of 47 Tuc remains unknown. The most variable known source in the field of 47 Tuc is classified as an M dwarf foreground star (see Sect. 5.2).

### 3.2. Spectral analysis

We performed an X-ray spectral analysis for the bright sources in the field of 47 Tuc, which their optical/infrared counterparts classified as a member of 47 Tuc (see Sect. 5.3). Also, the spectral analysis is performed for the most variable foreground star in the field of 47 Tuc (Src-No. 453; see Sect. 5.2). The spectra of the sources with a net source counts  $> 500$  in total have been extracted. We improved the statistics of the spectra by merging the spectra of all observations, in which the source was detected. Before merging the spectra of different observation, the variability of the source were checked to exclude the spectrum of the observation(s), in which the source shows a significantly different flux (see table B.1). We were able to fit the spectrum of sources using models for power-law (po), black-body (bb), collisionally-ionized thermal gas (apec, Smith et al. 2001), and X-ray emission from a hydrogen atmosphere of a neutron star (nsa, Zavlin et al. 1996) using Xspec (V.12.12.0). Figure 4 shows the spectrum of the X-ray sources and Table 3 the details of the models fitted to the spectrum of sources.

### 3.3. Hardness ratio

Hardness ratios (HRs) are useful tool for the study of spectral properties of X-ray sources. The HR and its error are defined as:

$$HR_i = \frac{B_{i+1} - B_i}{B_{i+1} + B_i} \text{ and } EHR_i = 2 \frac{\sqrt{(B_{i+1}EB_i)^2 + (B_iEB_{i+1})^2}}{(B_{i+1} + B_i)^2}, \quad (2)$$

respectively, where  $B_i$  is the count rate and  $EB_i$  is the corresponding error in the energy band  $i$ . We calculated the hardness ratio from the observation, in which the source had the highest detection likelihood. To increase the accuracy, we consider a HR measurement as significant only if the detection likelihood for the both corresponding energy bands was higher than 6 (i.e.  $> 3\sigma$ ). Table B.1 lists the HRs for all sources. Figure 3 shows the *eROSITA* sources with significant HRs. To understand the spectrum of sources, we plotted the lines representing the hardness ratios of different spectral models with various column densities from  $N_H = 10^{20} \text{ cm}^{-2}$  to  $N_H = 10^{23} \text{ cm}^{-2}$ . Four power-law models with photon-index  $\Gamma$  of 0.5, 1, 2, 3 correspond to hardness ratio of the hard sources, e.g. X-ray binaries, AGNs, or galaxies. Three apec model with the temperature of  $kT$  of 0.2, 1.0, and 2.0 keV represent the spectra of soft plasma emissions detected in sources like supernova remnants (SNRs), foreground stars, and symbiotic stars. As can be seen in the HR diagrams, foreground sources have a very soft spectrum. They have a very low  $N_H$ , which also is the reason why they appear much softer than the others. The majority of the sources are located around power-law models with  $\Gamma \sim 2 - 3$  in the energy bands  $< 2.3$  keV. As expected from the sensitivity of the *eROSITA* a few sources are significantly observed  $> 2.3$  keV. Considering these results, to calculate the X-ray flux of the sources, for which the spectrum have not been analysed in Sect. 3.2, we assumed an absorbed power-law model with a  $\Gamma = 3$  and a Galactic absorption of  $5.5 \times 10^{20} \text{ cm}^{-2}$  (i.e. Galactic adsorption in the direction of 47 Tuc, HI4PI Collaboration et al. 2016) (see Table B.1). We consider a source as soft source if it is detected significantly only in the first energy band. A source is classified as a hard source is it has significant emission in the highest energy band or in the last two higher energy bands. These sources can not be presented in the HR plots due to the lack of counts in bands necessary for the HRs or due to very large EHR. In Table B.1 these sources are classified as soft or hard X-ray sources.

## 4. Multi-wavelength studies of counterparts

We have searched for counterparts of the X-ray sources ( within their  $3\sigma$  positional error) in optical and infrared using the NWAY code, which is a Bayesian algorithm for cross-matching multiple catalogues provided by Salvato et al. (2018). In order to yield high accuracy, we only considered an infrared/optical counterpart for the X-ray source if the distance posterior probability, which is the probability computed using the Bayesian approach considering asymmetric parameters (e.g. positional uncertainties, distance of a counterpart from the X-ray source, and number densities) as it is explained in Salvato et al. (2018) in their Appendix B5, was higher than 50%. If both infrared and optical counterparts exist for a source, we checked if the position of optical and infrared counterparts are the same and it is from one source. Otherwise only the counterpart, which had a higher match distance probability and was closer to the position of the X-ray source is reported. To estimate the possibility of spurious matches we calculated the chance coincidence probability for the counterparts of X-ray sources in the field of 47 Tuc. We assumed a shift of  $10''$  in a random direction for the position of each source. The shifts are repeated four times. The probability of finding a new counterpart is considered as chance coincidence probability, which was  $(8.11 \pm 1.15)\%$  for the whole observational area. We also calculated the chance coincidence probability for those sources, which are located inside the  $18.8'$  circle area (where we have the highest exposure time of all observations) and for the sources outside this circle. It was

Table 3: Best-fit parameters of the X-ray spectra. Errors are at the 90% confidence level.

Src-No	Model	$N_{\text{H}}$ $10^{22} \text{ cm}^{-2}$	Photon index	Temperature	Abundance	$\chi^2$ (d.o.f)	Unabsorbed $F_{\text{X}}$ $10^{-14} \text{ erg s}^{-1} \text{ cm}^{-2}$	Unabsorbed $L_{\text{X}}^*$ $\text{erg s}^{-1}$
320	tbabs×(apec)	$1.85^{+0.59}_{-1.25}$	–	>1.32 keV	–	1.15 (10)	$5.20^{+0.88}_{-0.87}$	$1.23 \times 10^{32}$
	tbabs×(bb)	$0.65^{+0.74}_{-0.48}$	–	$0.64^{+0.38}_{-0.23}$ keV	–	0.950(11)	$1.3^{+1.16}_{-0.66}$	$2.90 \times 10^{31}$
	tbabs×(nsa)**	$0.78^{+0.81}_{-0.51}$	–	log(T): 6.48 K	–	0.961(11)	$0.89^{+0.42}_{-0.33}$	$2.11 \times 10^{31}$
340	tbabs×(bb+po)	$0.04^{+0.015}_{-0.01}$	$2.23^{+0.33}_{-0.30}$	< 0.90 keV	–	1.05 (116)	$12.38^{+1.10}_{-0.98}$	$2.80 \times 10^{32}$
	tbabs×(nsa+po)	<0.05	$2.06^{+0.08}_{-0.14}$	log(T): $5.8^{+0.13}_{-0.29}$ K	–	0.97 (116)	$9.27^{+0.27}_{-0.26}$	$2.14 \times 10^{32}$
341	tbabs×(apec+po)	< 0.19	$1.22^{+1.01}_{-0.38}$ keV	< 0.2	–	0.80 (24)	$1.61^{+0.14}_{-0.17}$	$3.82 \times 10^{31}$
453	tbabs×(apec+apec)	$0.020^{+0.02}_{-0.03}$	–	T1 : $0.28^{+0.09}_{-0.05}$ keV	$0.17^{+0.09}_{-0.06}$	1.07 (58)	$2.34^{+0.12}_{-0.11}$	$1.12 \times 10^{29***}$
				T2 : $1.04^{+0.09}_{-0.10}$ keV				
480	tbabs×(apec+apec)	$0.03^{+0.02}_{-0.01}$	–	T1 : $0.25^{+0.05}_{-0.04}$ keV	–	1.03 (38)	$5.80^{+0.36}_{-0.37}$	$1.37 \times 10^{32}$
				T2 : $4.27^{+1.59}_{-1.03}$ keV				
	tbabs×(bb+po)	$0.06^{+0.06}_{-0.05}$	$2.17^{+0.87}_{-0.96}$	< 0.66 keV	–	0.68 (38)	$3.92^{+0.54}_{-0.31}$	$9.01 \times 10^{31}$
481	tbabs×(bb)	$0.05^{+0.03}_{-0.02}$	–	$0.075^{+0.009}_{-0.008}$ keV	–	1.08 (30)	$1.65^{+0.18}_{-0.18}$	$3.90 \times 10^{31}$
	tbabs×(nsa)	$0.07^{+0.03}_{-0.02}$	–	log(T): $5.38^{+0.12}_{-0.08}$ K	–	1.09 (30)	$3.63^{+0.10}_{-0.11}$	$8.81 \times 10^{31}$
501	tbabs×(apec+apec)	$0.05^{+0.03}_{-0.02}$	–	T1 : $0.30^{+0.08}_{-0.60}$ keV	–	1.27 (80)	$6.14^{+0.26}_{-0.25}$	$1.49 \times 10^{32}$
				T2 : $5.41^{+13.2}_{-2.08}$ keV				
	tbabs×(nsa+po)	$0.04^{+0.04}_{-0.03}$	$1.45^{+0.41}_{-0.51}$	log(T): $6.24^{+0.42}_{-0.28}$ K	–	1.43 (81)	$6.27^{+0.34}_{-0.30}$	$1.45 \times 10^{32}$

\*: We assumed a distance of 4.45 kpc to estimate the X-ray luminosity of sources in 47 Tuc (see Sect. 1).

\*\* : Nonmagnetic neutron star atmosphere (nsa) model (Zavlin et al. 1996) has been applied for the systems, which have been candidate to have neutron star as their compact object. We assumed a mass and radius of  $M_{\text{NS}}=1.4M_{\odot}$  and  $R_{\text{NS}}=10$ . km for the neutron star as it has been used in nsa model for the QLMXBs and MSPs spectra (e.g. Bogdanov et al. 2006; Wijnands et al. 2005).

\*\*\* : For Src-No. 453, the distance of the counterpart, which is a foreground star located at  $\sim 200$  pc is considered.

( $5.73 \pm 1.55$ )% for the inner region and ( $8.47 \pm 1.89$ )% for the outer region. This result shows that by using the positional error of the merged observations (as explained in Sect. 2.3) we have lowered the chance coincidence probability in the crowded region of 47 Tuc. In order to decrease the consequences of spurious matches we applied additional criteria: we only accepted a counterpart of background galaxies/AGN or foreground star if the distance posterior probability of match was  $>70\%$ . For sources, which are classified as members of 47 Tuc the counterpart is accepted if it was located within  $2\sigma$  X-ray positional error. Moreover, the *Chandra* position has been used to search for infrared/optical counterpart (in the case that the source has a *Chandra* counterpart). These details are discussed in Sect. 5. In the next following sections, we discuss the multi-wavelength photometry used to uncover the stellar nature of our sources.

#### 4.1. Infrared counterparts of the sources

We searched for mid-infrared counterparts in the WISE All-Sky Survey in four energy bands (3.4, 4.6, 12, and 22  $\mu\text{m}$ , named  $W1$ ,  $W2$ ,  $W3$ , and  $W4$ , respectively; Cutri & et al. 2014). The extinction for the infrared WISE bands in the direction of 47 Tuc was negligible (Schlafly & Finkbeiner 2011). Table B.2 lists the magnitudes of WISE counterparts of the X-ray sources. Figure 5 shows the colour-colour diagram of the WISE counterparts of the X-ray sources in the field of 47 Tuc. The infrared colours shown in this plot can give us information about the na-

ture of the counterpart, i.e., whether the counterpart is a stellar object, an AGN, or a galaxy. The study of Wright et al. (2010) shows that background objects are usually expected to be red (i.e.  $W2 - W3 > 1.5$ ) in WISE colour, while stellar objects show a different colour (i.e.  $W2 - W3 < 1.5$ ). One can see that the counterparts of known background objects are separated from the X-ray sources with known stellar counterparts (see Sect. 5 and Fig. 5). We also checked if the X-ray sources have near-infrared counterparts in the 2MASS All-Sky Survey Catalogue in the three standard bands of  $J$ ,  $H$ ,  $K_s$  standard bands (Cutri et al. 2003). In the direction of 47 Tuc, we applied the extinction of 0.03, 0.02, 0.01 for the  $J$ ,  $H$ ,  $K_s$  bands, respectively (Schlafly & Finkbeiner 2011). In the colour magnitude diagram of the 2MASS counterparts (Fig. 6) we also show the position of the main isochrone of 47 Tuc, which was obtained using the theoretical models of the Dartmouth stellar evolution database (Dotter et al. 2008) for the age, metallicity, and distance of 47 Tuc as discussed in Sect. 1. As another key for the classification of symbiotic stars we considered the results of the machine learning method of Akras et al. (2019). They show that in the population of known symbiotic stars, the majority of systems appears to have  $J - H > 0.78$  and only a small fraction of S-type symbiotics behaves differently. The second criterion is  $K - W3 < 1.18$ , which separates the symbiotic stars significantly from the other types of sources. The second criterion might not apply for dusty symbiotic stars. In this case, there are two other criteria on the colours of  $H - W2 > 3.80$  and  $W1 - W4 < 4.72$ . We applied

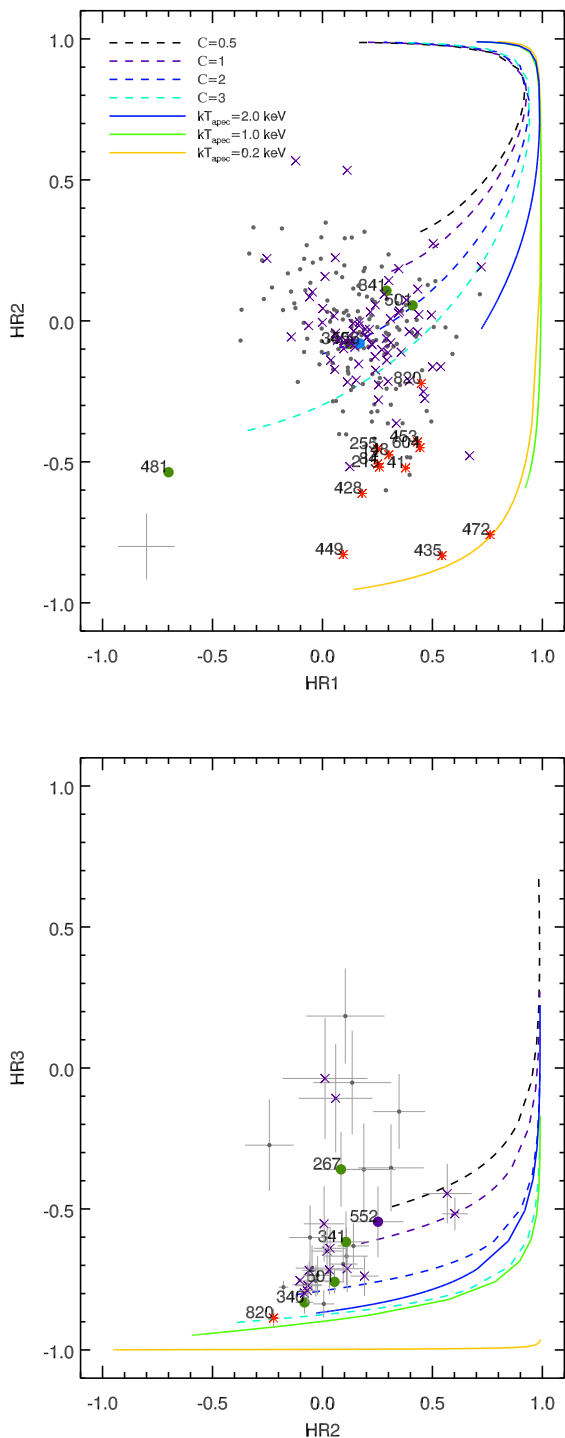


Fig. 3: Hardness ratio diagrams. The plotted hard lines are the hardness ratios calculated for different spectral models. As one can see in the upper plot there are sources in the foreground and therefore with very low  $N_H$ , they appear softer than the others. The symbols are the same as Fig. 2.

these criteria for the classification of symbiotic stars as we discuss in Sect 5.

#### 4.2. Optical counterparts of the sources

The most recent all-sky optical surveys, third Gaia Data Release (Gaia Collaboration 2020) and the first data release of the SkyMapper southern survey (Wolf et al. 2018), have been used to search for the optical counterparts of the eROSITA sources in the field of 47 Tuc. Table B.3 presents the Gaia and SkyMapper magnitudes of the optical counterparts of the X-ray sources. The SkyMapper catalogue includes photometric data in the energy bands from the optical to the near infrared. In SkyMapper survey we have mainly used the two known photometric magnitude bands ( $g$  ( $\lambda_{\text{eff}}=467$  nm) and  $r$  ( $\lambda_{\text{eff}}=616$  nm) to plot the colour magnitude diagram of the optical counterparts (see left diagram of Fig. 7). The Gaia surveys also report the magnitudes of the sources in three filter of  $G$  mag (roughly  $\lambda=300$  nm),  $G_{BP}$  ( $\lambda=400-500$  nm) mag, and  $G_{RP}$  ( $\lambda=600-750$  nm) (Gaia Collaboration et al. 2018), which have been considered in our study for the comparison with the SkyMapper magnitudes and for the Gaia colour magnitude diagram (see right diagram of Fig. 7). We also considered the Gaia-parallax measurement to identify foreground stars as presented in the work of Bailer-Jones et al. (2021).

The extinction of 0.12 and 0.09 has been applied for the  $g$  and  $r$  bands of SkyMapper. Also 0.18, 0.13, and 0.07 for  $G$ ,  $G_{BP}$ , and  $G_{RP}$  for the Gaia bands, respectively (Schlafly & Finkbeiner 2011). The theoretical isochrone line of 47 Tuc is also plotted for colour magnitude diagrams of SkyMapper and Gaia counterparts (Fig. 7) as it is explained in Sect. 4.1.

The logarithmic X-ray to optical flux ratio  $\log(\frac{F_X}{F_{\text{opt}}})$ , versus the X-ray flux and also HR2

(see Sect. 3.3) are shown in Figure 8. The modified version of the flux ratio equation  $\log(\frac{F_X}{F_{\text{opt}}})$  (Maccacaro et al. 1988) with an average of  $G_{BP}$  and  $G_{RP}$  Gaia magnitudes is applied:

$$\log\left(\frac{F_X}{F_{\text{opt}}}\right) = \log_{10}(F_X) + \frac{G_{BP} + G_{RP}}{2 \times 2.5} + 5.37, \quad (3)$$

where  $F_X$  is the X-ray flux and  $g$  and  $r$  are the SkyMapper magnitudes of the optical counterpart associated with the X-ray source. As Figure 8 shows, the main part of the classified sources of 47 Tuc are more dominant in optical radiations.

#### 4.3. Catalogues of AGNs and galaxies

The following catalogues were cross-checked with all X-ray sources to find the classified background objects in available catalogues:

- The Million Quasars (Milliquas) Catalogue (Flesch 2019)
- Quasar and galaxy classification in 2nd Gaia Data Release (Bailer-Jones et al. 2019)
- The UV-bright Quasar Survey (Monroe et al. 2016)
- The SWIFT AGN and Cluster Survey (Dai et al. 2015)
- Identification of 1.4 Million AGNs in the mid-Infrared using WISE Data (Secrest et al. 2015)
- Identifications of AGNs from the WISE, 2MASS, and ROSAT All-Sky Surveys (Edelson & Malkan 2012)

#### 4.4. Catalogues of members of the 47 Tuc

Sources, which are located on the principal sequence of optical and infrared colour magnitude diagrams (see Fig. 6 and Fig.7) and are listed in the following catalogues, were confirmed as members of 47 Tuc:

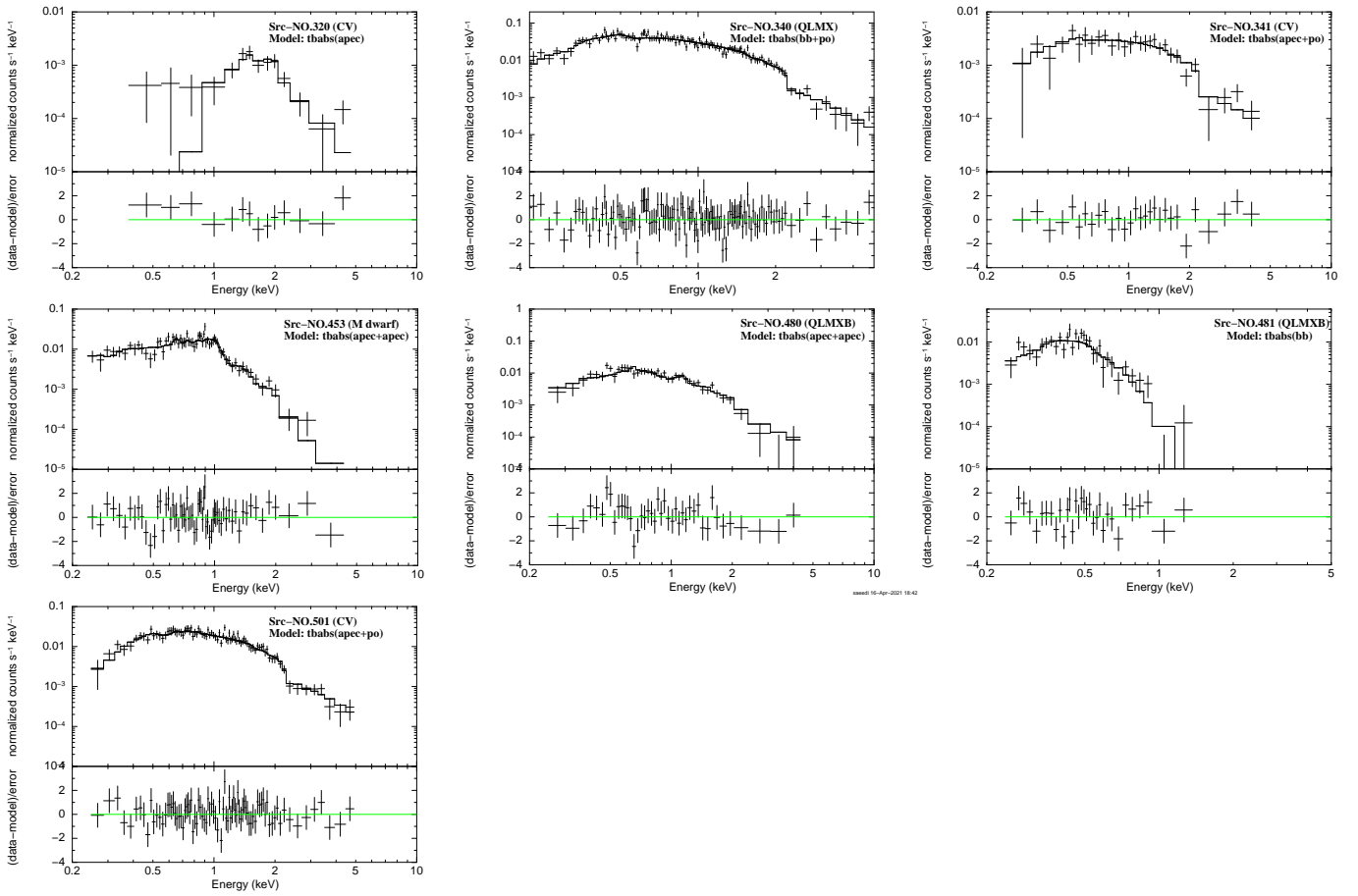


Fig. 4: Combined spectrum of *eROSITA* observations of the X-ray sources

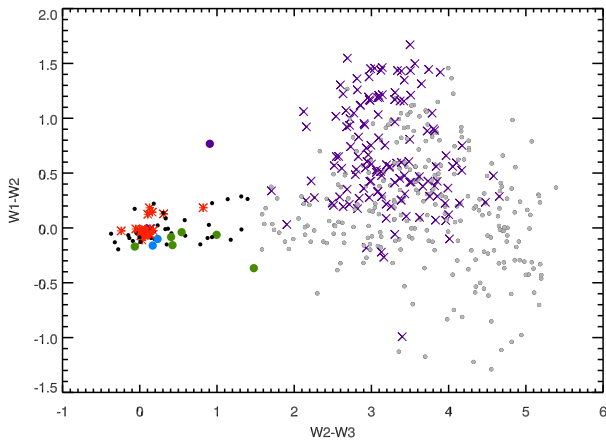


Fig. 5: Colour-colour diagram of mid-infrared WISE ( $W1-W2$  versus  $W2-W3$ ). The symbols are the same as Fig. 2. The sources, which had a WISE counterpart with an upper limit in  $W2$ , or  $W3$ , or both are shown with gray circles.

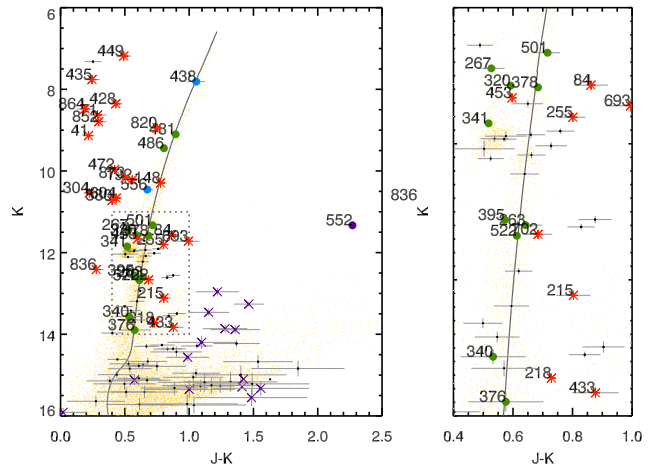


Fig. 6: The colour-magnitude diagram of 2MASS counterparts of the X-ray sources in the field of 47 Tuc. To have a better look into the crowded region the left plot shows a zoom to the dashed square in the right plot. The yellow dots are all 2MASS sources detected in the field of 47 Tuc. The symbols are the same as Fig. 2.

- Catalogue of [Cordero et al. \(2014\)](#) present the detailed of the abundances of 164 RGB Stars in the 47 Tuc.
- [Carretta et al. \(2013\)](#) provides the aluminium abundances for a sample of about 100 RGBs in 47 Tuc and M4 GCs.
- The work of [Gratton et al. \(2013\)](#) presents analysis of the composition 110 red horizontal branch stars in 47 Tuc.

- Based on various parameters e.g. the metallicity and radial velocity, the membership of more than 43000 sources in the



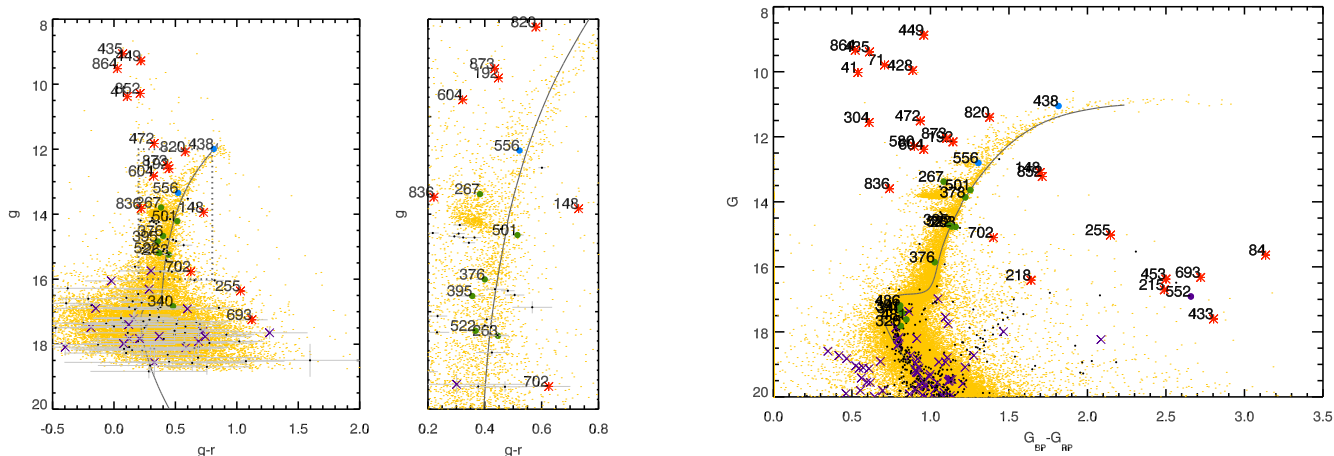


Fig. 7: The optical counterpart of the X-ray sources in the field of 47 Tuc observed by SkyMapper (Wolf et al. 2018) (left panel) and Gaia third data released (Gaia Collaboration 2020) (Right panel). The yellow dots are all optical sources detected in the field of 47 Tuc dSph and the gray hard lines are the theoretical isochrone of The Dartmouth stellar evolution database (Dotter et al. 2008) for the age, metallicity, and distance of 47 Tuc (see Sect. 1). The rest of the symbols are the same as Fig. 2. To have a better look into the crowded region of Skymapper colour-magnitude diagram a zoom to the dashed square is shown.

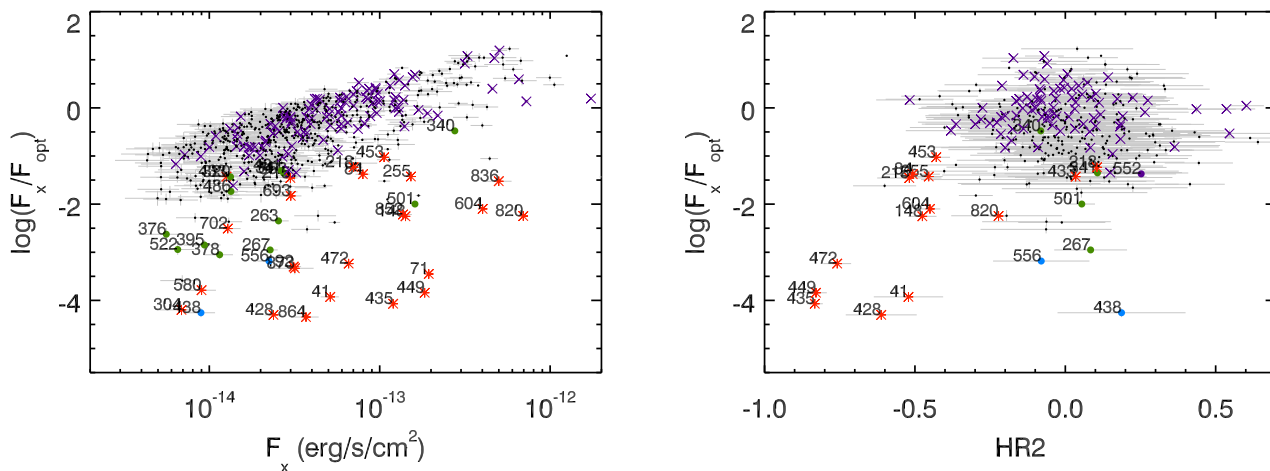


Fig. 8: Logarithmic X-ray to optical flux ratio  $\log(\frac{F_x}{F_{opt}})$  versus the maximum X-ray flux (left) and HR2 (right) for the sources in the field of 47 Tuc. The symbols are the same as Fig. 2.

field of GCs including 47 Tuc are investigated. Lane et al. (2011).

## 5. Discussion

The procedure for the classification of the X-ray sources using the above results is explained the the following:

### 5.1. Classification of background sources in the field of 47 Tuc

For the classification of AGNs in the field of 47 Tuc, we mainly used the criteria, which have been defined in the study of Wright et al. (2010) (see Sect. 4.1). The X-ray sources with a WISE counterpart (with >70% probability to be a match to the X-ray source), which have significant magnitudes in  $W1$ ,  $W2$ ,  $W3$  bands and fulfil the condition of  $W2 - W3 > 1.5$  are considered as background sources. In this classification, we excluded the sources, which have only an upper limit magni-

tude in the bands  $W2$  and/or  $W3$  of their WISE counterpart. These sources remain unclassified since WISE counterpart in the colour of  $W2 - W3$  could not be significantly considered as a background object. Moreover, we cross-correlated all available AGN/quasar/galaxy catalogues (see Sect. 4.3) with our catalogue to classify the other known X-ray background sources. Almost all the classified background objects in other available catalogues had a WISE counterpart satisfying the condition of  $W2 - W3 > 1.5$  as well. We ended up with the classification of ninety-two AGNs/galaxies in the field of 47 Tuc. Fig. 9 shows the distribution of classified background sources. They are mainly located outside the region, where most of the X-ray members of 47 Tuc are detected (i.e.  $\geq 12'.0$ ). Fig. 8 also shows that the classified AGNs have a higher relative X-ray flux than the X-ray sources in 47 Tuc and the foreground stars.



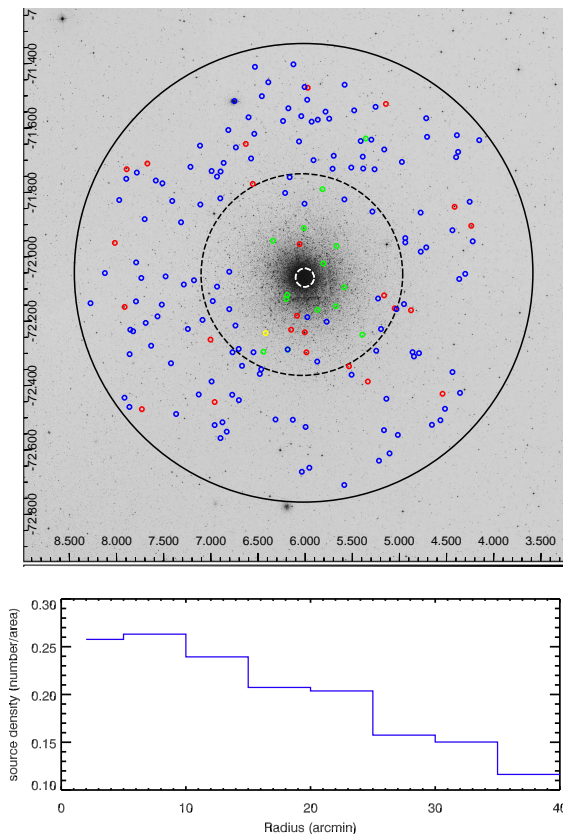


Fig. 9: **Upper image:** The optical image of the field of 47 Tuc observed by DSS survey (red filter) (Bacher et al. 2005). Hard black region shows the total area which have been observed by *eROSITA* (radius of 42'). Dashed black region is the area which was if the field of view of all observations and have been used for the XLF calculation (radius of 18'.8). The dashed white region is the area, where the observation of *eROSITA* was unresolved and have been excluded in this study (radius of 1'.7). The position of classified AGNs, foreground stars, and accreting binaries are shown by blue, red, and green circles, respectively. The single source classified as a XRB in SMC is in yellow. **Lower plot:** Normalized source density versus the radius of the field of view of *eROSITA* observation. No sources are detected for radius <2.' due to the large unresolved source in the center.

## 5.2. Classification of foreground stars/systems in the field of 47 Tuc

For the classification of the foreground stars/systems we consider three main criteria for the infrared/optical counterpart of the X-ray source: (having >70% distance match probability to the X-ray source), being a stellar object according to the WISE colours (see Sect. 4.1), and/or the distance of optical counterpart according to the Gaia parallax measurement shows that the source is a foreground object in the field of 47 Tuc (Bailer-Jones et al. 2018). The colour magnitude diagrams of the counterparts of 2MASS (Fig. 6), SkyMapper, and Gaia (Fig. 7) show that the position of the classified foreground stars are located outside the main sequence of the 47 Tuc. As Fig. 2 shows, **Src-No. 453** is the most variable foreground stars. The source seemed to be in the flaring state in four first observations, as its count rate drops down in OBS 5 (see Table B.1). We combined all the data of four observations and fit the spectrum with two absorbed plasma models (see Table 3 and Fig. 4). The X-ray spectrum

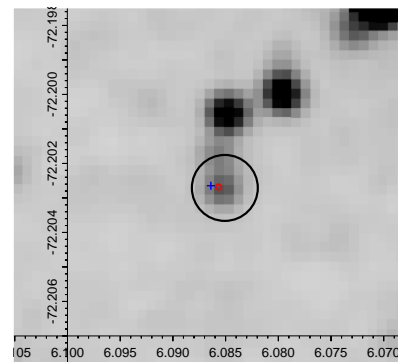


Fig. 10: The Infrared 2MASS ( $k_s$  band) image of the position of Src-No. 453, which is classified as a foreground M dwarf. regions show  $3\sigma$  positional error of X-ray source (black) and infrared 2MASS counterpart (red). The blue cross shows the position of optical Gaia counterpart.

Table 4: Characteristic of low luminosity X-ray sources (AWDs, XRBs, and contact binaries)

Source class	Spectral emission keV	Luminosity $\text{erg s}^{-1}$
Symbiotic: $\alpha$ -type	<0.5	$L_{bol} > 10^{36}$
Symbiotic: $\beta$ -type	<2.4	$L_x \sim 10^{30-32}$
Symbiotic: $\delta$ -type	>2.4	$L_x \sim 10^{31-34}$
Symbiotic: $\gamma$ -type	>2.4	$L_x > 10^{34}$
CV: Non-magnetic	2–5.	$L_x \sim 10^{29-32}$
CV: Polars	<5.0	$L_{bol} \sim 10^{30-31}$
CV: Intermediate polars	5–50.	$L_x < 10^{34}$
Quiescent LMXBs	<5.	$L_x \sim 10^{31-33}$
Millisecond pulsars	0.2–2.5	$L_x \sim 10^{30-31}$
Active binaries	<2.5	$L_x \sim 10^{29-32}$

is very similar to that of stellar object, also the measured column density is lower than the Galactic absorption in the direction of 47 Tuc (i.e.  $5.5 \times 10^{20} \text{ cm}^{-2}$ ), which is expected from a foreground star. Considering the infrared and optical colours of the source counterpart ( $J - H = 0.44 \pm 0.12$ ,  $H - K_s = 0.25 \pm 0.13$ ,  $i - z = 0.49 \pm 0.05$ , and  $z - J = 1.52 \pm 0.07$ ), it can be classified as an early type M dwarf (M0–M3, West et al. 2011). Figure 10 shows the infrared 2MASS ( $k_s$  band) image of the counterpart of Src-No. 453.

## 5.3. X-ray sources in 47 Tuc

The majority of X-rays sources of GCs are expected to be low luminosity ( $< 10^{33} \text{ erg s}^{-1}$ ) X-ray sources, which can be quiescent LMXBs, different types of AWDs, MSPs, and magnetically active binary systems. In the following, we briefly review the X-ray spectra and luminosity of these sources. Also, Table 4 summarises the properties of X-ray spectrum and luminosity of all types of the sources.

One of the major class of X-ray sources in GCs is AWDs. They can be symbiotic stars, which have a red giant branch (RGB) star as the companion of the white dwarf, or cataclysmic variables (CVs), which are systems made of a white dwarf with a main sequence companion (Mukai 2017).

**Symbiotic stars:** These systems are categorised into the four types of  $\alpha$ ,  $\beta$ ,  $\gamma$ , and  $\delta$  (Luna et al. 2013). In the  $\alpha$ -type symbi-

otics the X-ray emission originates from the quasi-steady burning of the material transferred from the red giant via Roche lobe overflow onto the surface of the WDs. The emission is detected  $<0.5$  keV, which is the reason to call them supersoft sources. Supersoft sources are bright mainly in the UVs and very soft X-rays with a bolometric luminosity  $>10^{36}$  erg  $s^{-1}$ .  $\beta$ -type symbiotics have the main X-ray emission  $<2.4$  keV ( $L_x \sim 10^{30-31}$  erg  $s^{-1}$ ), which most likely arises from the collision of the wind of the WD with the wind of the red giant. Observations show that the X-ray luminosity can be around two orders of magnitudes higher, when the system is in the outburst (Luna et al. 2013).  $\delta$ -type symbiotics are highly absorbed hard X-ray sources ( $>2.4$  keV,  $L_x \sim 10^{31-34}$  erg  $s^{-1}$ ). Theoretical models suggest that the X-ray emission originates from the boundary layer between the accretion disk and the WD (e.g. Luna et al. 2013). There is also a class of  $\beta/\delta$ -type symbiotics, which have both soft and hard components. For these types of symbiotic stars usually one or two ionised plasma model(s) have been used to fit to the spectra (e.g. Luna et al. 2013). The  $\gamma$ -type symbiotic stars (symbiotic X-ray binaries) are actually a subclass of LMXBs, in which the binary system consists of a red giant and a neutron star (as the mass accretor). The main part of the emission of these sources is hard ( $>2.4$  keV) and can have a high X-ray luminosity ( $L_x > 10^{34}$  erg  $s^{-1}$ ).

**CVs:** There are two main classes of the CVs, magnetic and non-magnetic CVs. In the non-magnetic CVs, a disk forms around the WD, however the disk is not hot enough to produce X-ray emission, therefore, the disk, by itself, is not visible in X-rays. On the other hand, the boundary layer between the disk and the surface of the WD produces X-ray emission with temperatures of few keV and X-ray luminosities between  $L_x \sim 10^{29-32}$  erg  $s^{-1}$  (e.g. Mukai 2017; Kuulkers et al. 2006; van Teeseling et al. 1996). Magnetic CVs can be divided into two sub-classes of polars and intermediate polars. Polars are systems without an accretion disk, where the materials reach to the surface of WD following the magnetic field lines (Mukai 2017). *XMM-Newton* observations show that polars are usually soft ( $<5.0$  keV) and very faint X-ray sources with a bolometric luminosity of  $\sim 10^{30}$  erg  $s^{-1}$  (e.g. Ramsay et al. 2004). Intermediate polars have the dominant emission in hard X-rays (5-50 keV,  $L_x < 10^{34}$  erg  $s^{-1}$ ; e.g. Suleimanov et al. 2019), which is produced by a strong shock above the poles of WDs, where a noticeable amount of materials from the inner part of the truncated accretion disk follow the magnetic field lines. They also can show soft X-ray emission, which are orders of magnitude fainter than that of hard X-rays (Mukai 2017; Balman 2012). Mukai (2017) shows that in general CVs have  $\log(\frac{F_x}{F_{opt}}) < 1.0$  and magnetic CVs usually have larger  $\log(\frac{F_x}{F_{opt}})$  than non-magnetic CVs. The temperature of the soft X-ray emission of CVs can be estimated using the plasma atmosphere models (e.g. Worpel et al. 2016; Haberl et al. 2002).

**Quiescent LMXBs:** A black hole or a neutron star forms a binary systems with a late type low mass star ( $<1.0M_{\odot}$ ) (Bernardini & Cackett 2014). Observational studies show that quiescent LMXBs are X-ray sources with soft X-ray mission ( $<5.0$  keV) and X-ray luminosities  $\sim 10^{30-33}$  erg  $s^{-1}$  (e.g. Campana et al. 1998; Yokogawa et al. 2000; Jonker et al. 2007). The X-ray spectrum of QLMXBs can be fitted with a black-body or a neutron star atmosphere model or has a hard power-law component (e.g. Wijnands et al. 2005). A radius of 1–2 km (fitting with a black-body model, Brown et al. 1998) or 10–12 km (fitting with neutron star atmosphere models, e.g. Rutledge et al. 2002; Heinke et al. 2003) are expected to be inferred from the models.

**MSPs:** They are known to be fast spinning neutron stars in a binary system with a low mass companion ( $<1. M_{\odot}$ ) mainly detected in GCs. According to the recycling scenario, an old neutron star in an LMXBs spins up by accreting matter from the companion. The spun-up neutron star is still visible in X-rays when the accretion phase ends due to the detachment of the companion and/or when the companion has lost its atmosphere (e.g. Di Salvo & Sanna 2020). Detached MSPs in general have soft X-ray emission of 0.5–2.5 keV and  $L_x \sim 10^{30-31}$  erg  $s^{-1}$  (e.g. Bhattacharya et al. 2017; Becker & Trümper 1999). There are rare cases of isolated pulsars, which show a slightly harder spectrum (e.g. Mereghetti et al. 2016). Therefore, in general, they can be distinguished from the quiescent LMXBs which have  $L_x \sim 10^{31-33}$  erg  $s^{-1}$ . The emission of the MSPs comes from a smaller region than that of QLMXBs: the radius inferred from a black-body model, or neutron star atmosphere model, fit to the X-ray spectrum of MSPs is  $\sim 0.1$ – $0.3$  km, or  $\sim 0.5$ – $0.2$  km, respectively. (e.g. Bogdanov et al. 2006).

**Active binary systems:** Magnetically active binary systems (e.g. RS Canum Venaticorum, or BY Draconis, etc) consist of at least one (sub)-giant (RS CVn systems), or two main sequence stars (BY Dra systems) (e.g. Dempsey et al. 1993a). The X-ray emission in these systems is caused by the strong magnetic activity, induced by rapid rotation in close binary system (e.g. Dempsey et al. 1997) and tend to have soft spectrum often with  $KT < 2.5$  keV. BY Draconis are in general observed with a low X-ray luminosity of  $10^{29-31}$  erg  $s^{-1}$  (e.g. Dempsey et al. 1997; Heinke et al. 2005). RS CVn systems have several cases with luminosity  $< 10^{31}$  erg  $s^{-1}$ , however, they can be observed at higher luminosities as well (e.g. Rengarajan & Verma 1983; Dempsey et al. 1993b). It also has to be considered that in these *eROSITA* observations, we only detected sources with X-ray luminosities  $L_x \gtrsim 10^{31}$  erg  $s^{-1}$ . Therefore, only luminous and high temperature active binaries are observed, which can show higher temperatures of  $\sim 3.5$  keV (e.g. Dempsey et al. 1993b).

The details of the spectrum and luminosity of X-ray sources together with the multi-wavelength information of their counterpart help to classify low luminosity X-ray sources. As an example, Pooley et al. (2003) have suggested a way to distinguish the quiescent LMXBs from the other types of low luminosity X-ray sources in GCs: only AWDs and quiescent LMXBs have  $L_x > 10^{32}$  erg  $s^{-1}$ , while the quiescent LMXBs show much softer X-ray spectrum than that of AWDs. Therefore, quiescent LMXBs can be distinguished from the rest of the sources. Moreover, the spectral model is useful for the classification of MSPs and QLMXBs. If the spectrum of a source is fitted with either a black-body and/or a neutron star atmosphere model component in such way that a reasonable radius can be inferred from the model(s), the source is rather a QLMXB or a MSPs candidate than a CV, for which we expect its soft spectrum to be fitted better with a plasma atmosphere model. The radii of black-body model and/or neutron star atmosphere model would help to characterise the neutron star.

The faintest object detected by *eROSITA* in the field of 47 Tuc is Src-No.330 with a flux of  $\sim 4.6 \times 10^{-15}$  erg  $s^{-1} \text{cm}^{-2}$  (assuming located at the distance of 47 Tuc:  $L_x = 9.9 \times 10^{30}$  erg  $s^{-1}$ ). Therefore, in principle we are able to observe different types of low luminosity X-ray sources of 47 Tuc with  $L_x > 10^{31}$  erg  $s^{-1}$ . In order to be more precise in the classification of members of 47 Tuc, we only confirm an optical/infrared source as the counterpart for the X-ray source if it is within the  $2\sigma$  X-ray positional error circle and if there are no multiple candidates as counterparts in the error circle. Fig. 7 and Fig. 6 show diagrams of the properties of the near-infrared

and optical counterparts of the X-ray. The sources, which have a counterpart as a star on the main sequence or on the RGB in 47 Tuc are marked in blue and green circles, respectively. All these counterparts are confirmed as members of 47 Tuc (Lane et al. 2011) and the blue sources are also classified as red giants (e.g. Cordero et al. 2014) (see Sect. 4.4). We double checked the position of the X-ray source with the *Chandra* position in case the sources was detected with *Chandra* as well to improve the positional accuracy for the counterpart selection. Figure A shows infrared 2MASS images of the position of these X-ray sources. Based on the X-ray analysis we classify the sources as it is explained in the following:

### 5.3.1. Sources with an RGB counterpart

Following X-ray sources have an RGB counterpart (Cordero et al. 2014; Carretta et al. 2013), which is classified as a member of 47 Tuc. They are candidates for different types of symbiotic stars or RS CVn active binaries in 47 Tuc:

**Src-No. 438:** The brightest RGB counterpart belongs to this source (see Fig. 6 and Fig. 7). The counterpart is a known asymptotic giant branch star in 47 Tuc (Cordero et al. 2014) and located in  $2\sigma$  error circle of the X-ray source. The X-ray luminosity of the source is  $L_x \gtrsim 10^{31} \text{ erg s}^{-1}$  and the only significant hardness ratio is  $HR2 = 0.19 \pm 0.21$ , which means that the source is mainly detected in 0.6-2.3 keV. The infrared WISE and 2MASS counterparts suggest colours of  $J - H = 0.90 \pm 0.06$  and  $K - W3 = 0.11 \pm 0.03$  for the source, which agrees well with the infrared colours of the symbiotic stars (see Sect. 4.1). Therefore, the source is a candidate for a symbiotic star in 47 Tuc.

**Src-No.556:** The sources with an X-ray luminosity of  $L_x \sim 4 \times 10^{31} \text{ erg s}^{-1}$  can be a candidate for either a symbiotic star or an active binary (RS CVn type). According to the hardness ratios the main part of the X-ray emission is  $< 2.4$  keV. The source has a *Chandra* counterpart. According to *Chandra* position the red giant counterpart is located within  $2\sigma$  positional error and the *eROSITA* position show the the red giant is overlapped with  $2\sigma$  X-ray positional error (see Fig. A). The red giant counterpart has a colour of  $J - H < 0.78$ , which clarifies that the source has a low chance of being a symbiotic star (see Sect. 4.1). It is more likely a candidate for RS CVn contact binary.

### 5.3.2. Sources with a counterpart in the main sequence

Sources that have an optical or infrared counterpart on the main-sequence are marked with green circles in the colour magnitude diagrams (see Fig. 7 and Fig. 6). These diagrams show that the sources are located on the main sequence of 47 Tuc. In general, with a main sequence counterpart, low luminosity X-ray sources are candidates for quiescent LMXBs, MSPs, CVs, or active binary systems.

**Src-No.263, Src-No.376, Src-No.395, src-No.486, Src-No.522:** They are only detected in one or two observations. The HRs of these sources were not significant. The infrared and optical counterpart of these sources confirmed as a member of 47 Tuc within  $1-2\sigma$  X-ray positional error (McDonald et al. 2011; Lane et al. 2011; Narloch et al. 2017). According to their X-ray luminosities ( $\sim 10^{31} \text{ erg s}^{-1}$ ) they can be candidates for either active binaries in a flare state or faint, variable, and non-magnetic CVs.

**Src-No.267:** The optical/infrared counterpart of the source, which is located which in  $1\sigma$  X-ray positional error is already classified as a peculiar star (Cl\* NGC 104 LEE 2531; Wenger

et al. 2000) and a member of 47 Tuc (McDonald et al. 2011). The optical and infrared colour magnitude diagrams show that the counterpart located in horizontal branch of 47 Tuc (see Fig. 7 and Fig. B.2). The HR diagrams shows that the source it is hard source and its luminosity ( $L_x \sim 10^{32} \text{ erg s}^{-1}$ ) suggest that it can be candidate for either a non-magnetic CV or QLMXB. Considering the significant emission above  $> 2.0$  keV it can not be a candidate for an active binary.

**Src-No.320:** Source has no infrared counterpart. Its optical counterpart, which is located  $2.4''$  away from the X-ray position is considered as a post-main sequence star in 47 Tuc (McDonald et al. 2011) and the Gaia colour magnitude diagram shows it on the main sequence (see Fig. 7). The spectrum of the source is highly absorbed in soft X-rays and has the main emission  $> 1$  keV (Fig. 4 and Table 3). The source shows no X-ray variability and has an absorbed  $L_x \sim 1.8 \times 10^{31} \text{ erg s}^{-1}$ . The spectrum is too hard to make it an active binary candidate. We tried to fit the spectrum with an absorbed black-body model and also an absorbed nsa model (see Table 3). An absorbed black-body model suggest a radius of  $< 0.1$  km, and an absorbed nsa model an effective radius of  $< 0.8$  km, which are both typical for MSPs using these two models (see Sect. 5.3), while the temperatures of these two models are much higher than those of MSPs (Bogdanov et al. 2006). Therefore the possibility that the compact object is a neutron star is very low. The source is most probably a CV candidate.

**Src-No.340:** The optical/infrared counterpart of Src-No.340 is a main sequence star considering  $2\sigma$  *Chandra* and *eROSITA* positional errors of the source (see Fig. A) and classified as a member of 47 Tuc (McDonald et al. 2011). We tried different models for the spectrum of the source. The best fit is with an absorbed black-body plus a power-law tail (Table 3 and Fig. 4). The black-body model and the nsa model suggest a radius of  $< 1.54$  km and  $13.5_{-5.6}^{+13.2}$  km, respectively, which are both reasonable enough to assume the source as candidate for QLMXBs. Considering the counterpart, luminosity, and the X-ray energy range source is a candidate for QLMXBs.

**Src-No.341:** The main emission of the source is detected between 0.5–5.0 keV with an X-ray luminosity of  $\sim 4 \times 10^{31} \text{ erg s}^{-1}$ . There is no infrared counterpart for the source. There is a Gaia counterparts within the  $1\sigma$  positional error of the X-ray source, which is located on the main sequence of 47 Tuc. This counterpart is also classified as a member of 47 Tuc (Narloch et al. 2017). We tried to fit the spectrum with a absorbed black-body plus a power-law model (for the hard tail component), which was failed. It was also unsuccessful while trying nsa model. Therefore, the possibility that Src-No.341 is either a MSPs with a hard power-law tail or a QLMXB is very low (see the discussion in Sect. 5.3). Moreover, we could not fit the spectrum with two ionised plasma model components as observed in the spectrum of bright active binaries. The hard tail of the spectrum ( $> 2.0$  keV), which is best fit with a power-law model with a photon index  $< 2.0$  suggests that it is more likely a CV candidate rather than an active binary.

**Src-No.378:** The counterpart of the source, which is located within  $1\sigma$  positional error is classified as a member of 47 Tuc but not as an RGB star in available catalogues (see Sect. 4.4). However, The position of the source in infrared colour-magnitude diagram suggests that the counterpart is on RGB (see Fig. 6). Also, the position of the Gaia counterpart in optical colour magnitude diagrams shows that it is about to leave the main sequence (see Fig. 7). The study of infrared colours of the source shows that  $J - H < 0.78$  and thus, the possibility of being a symbiotic star is very low (see Sect. 4.1) The source was bright enough



Table 5: List of the X-ray sources, which are members of 47 Tuc

NO	RA (J2000)	DEC (J2000)	r1 $\sigma$ (")	count-rate (0.2–5. keV) (cts s <sup>-1</sup> )					Var	Note <sup>†</sup>
				OBS1	OBS2	OBS3	OBS4	OBS5		
263	00 21 37.25	-71 38 59.8	2.52	–	0.007± 0.001	–	–	–	–	CV/active binary
267	00 21 40.94	-72 15 38.4	0.98	–	0.007± 0.001	0.008 ± 0.002	–	0.006 ± 0.001	1.33± 0.29	CV
320	00 22 26.07	-72 06 49.2	1.15	–	0.003± 0.001	0.004± 0.289	0.003± 0.001	0.004± 0.001	1.30± 68.06	CV
340	00 22 45.28	-71 59 08.3	1.20	0.066± 0.008	0.076± 0.002	0.074± 0.003	0.074± 0.002	0.067± 0.002	1.15± 0.15	Quiescent LMXB
341	00 22 46.04	-72 10 22.8	0.70	0.011± 0.299	0.008± 0.001	0.009± 0.001	0.007± 0.001	0.008± 0.001	1.67± 26.23	CV
376	00 23 16.89	-72 02 24.3	2.21	–	–	–	–	0.002± 0.001	–	CV/active binary
378	00 23 19.20	-71 48 26.9	2.05	–	0.006± 0.001	–	0.003± 0.001	–	1.76± 0.41	CV/active binary
395	00 23 31.36	-72 11 00.4	2.48	–	–	0.003± 0.001	0.004± 0.001	–	1.70± 0.51	CV/active binary
438	00 24 03.66	-71 55 48.0	1.60	–	0.002± 0.001	–	0.002± 0.000	–	1.63± 0.49	Symbiotic star
480	00 24 43.35	-72 18 25.50	1.30	0.022± 0.004	0.032± 0.003	0.022± 0.001	0.028± 0.003	0.021± 0.001	1.57± 0.15	Unclassified
481	00 24 44.21	-72 08 19.0	1.16	–	0.006± 0.001	0.007± 0.001	0.007± 0.001	0.008± 0.001	1.19± 0.26	Quiescent LMXB
486	00 24 45.96	-72 08 59.0	2.95	–	0.004± 0.001	–	–	–	–	CV or active binary
501	00 24 56.97	-72 06 51.8	1.5	0.047± 0.005	0.042± 0.002	0.044± 0.002	0.041± 0.002	0.045± 0.002	1.14± 0.15	CV
522	00 25 18.95	-71 58 00.9	2.40	–	–	–	0.002± 0.000	–	–	CV or active binary
556	00 25 43.48	-72 18 52.1	1.52	–	–	0.005± 0.001	–	0.006± 0.001	1.33± 0.29	RS CVn

for neither spectral analysis nor HR study. X-ray luminosity of  $L_x \sim 4 \times 10^{31} \text{ erg s}^{-1}$  suggests that it can be a CV or an active binary.

**Src-No. 480:** *eROSITA*  $2\sigma$  positional error of Src-No.480 shows no counterpart, while the *Chandra*  $2\sigma$  positional error shows a main sequence counterpart for the source classified as a member of 47 Tuc (McDonald et al. 2011). There is also a red giant belong to 47 Tuc (McDonald et al. 2011), which has an overlap with  $2\sigma$  positional error of both *eROSITA* and *Chandra* (see Sect. A). It can not be clear if the emission is correlated with either the main sequence star or the red giant counterpart. We tried to fit the spectrum with different models. The best fit is obtained assuming two component *apec* model, which is similar to the spectra of the symbiotic stars. As Table 3 shows the black-body plus power-law model does not fit well to the spectrum. Ineligible result was the same when we applied the *nsa* model. These facts make the nature of the source unclear if it is a symbiotic star, QLMXBs, or a CV. Therefore, we kept this source unclassified.

**Src-No. 481:** The spectrum of the source is soft (see Fig. 4 and Table 3). The *eROSITA* position shows only a *Chandra* counterpart, which also is considered to search for optical/infrared counterparts for the source. There was an optical counterpart within the  $2\sigma$  positional error (see Fig. A). The counterpart is a star reported as a 47 Tuc members (Cohen et al. 2015). We tried both black-body and *nsa* models for the spectrum (see Table 3). The radius of emitting surface using the absorbed black-body model is  $3.6^{+2.8}_{-1.3} \text{ km}$ , and using the *nsa* model is  $23^{+11}_{-13}$ , which makes this source a candidate for a QLMXB (e.g. Heinke et al. 2003).

**Src-No. 501:** The source has a *Chandra* counterpart. The position and positional error of *Chandra* has been considered to search for the counterpart as well. Infrared/optical counterparts are located within  $2\sigma$  of the X-ray positional error of *eROSITA* and  $3\sigma$  of *Chandra* X-ray source. The spectra of the source (Fig. 4 and Table 3) is fitted well with an absorbed two component thermal model ( collisionally ionized diffuse gas model, *apec*, Smith et al. 2001). According to the counterpart (, which is about to leave the main sequence) and luminosity ( $> 10^{32} \text{ erg s}^{-1}$ ), it is either a CV or QLMXB candidate. The spectrum of the sources is fitted well with two *apec* models (see Fig. 4 and Table 3), while the attempt to fit it with an absorbed black-body and

power-law model was problematic. We fitted an absorbed neutron star atmosphere model plus a power-law component to the spectrum. However, the temperature of neutron star atmosphere model was too high to yield a reasonable neutron star radius (see Sect. 5.3). Therefore, the source is rather a CV candidate.

#### 5.4. other sources:

**Src-No. 552:** The source has a counterpart in optical and infrared located within  $2\sigma$  positional error of *eROSITA* and  $3\sigma$  positional error of *Chandra* (see Fig. A). The counterpart is already classified as the Mira star in the catalogue of long period variable stars of Small Magellanic Cloud (SMC) (Soszyński et al. 2011) and as optical/infrared colour magnitude diagrams show (see Fig. 6 and Fig 7), it is not in the population of 47 Tuc. The HRs show that the source should be observable in hard X-ray ( $> 2.0 \text{ keV}$ , see Fig. 3) and the luminosity of the source assuming a distance of 62.4 kpc for SMC is  $\sim 10^{34} \text{ erg s}^{-1}$ , which makes a candidate for an X-ray binary in SMC.

#### 5.5. X-ray luminosity function (XLF)

*Chandra* observation of 47 Tuc was limited to the central region with a radius of  $2'.7$  (See Sect. 1), while *eROSITA* observation gives an opportunity to study a large area surrounding this GC. In order to provide a more comprehensive view of the population of X-ray binaries in 47 Tuc, we calculated the XLF of the central annular area with inner and outer radii of  $1'.7$  and  $18'.8$ , respectively (see Fig. 1). The inner region is excluded since there is only an unresolved emission from the X-ray sources located within  $1'.7$  central region of 47 Tuc in *eROSITA* observations. The outer radius includes the area, which is covered by all observations and is therefore expected to have an almost uniform exposure time. In the first step, we ran source detection for the merged event files of all observations in the energy band of 0.5–2.0 keV. The sources, which have been classified as foreground stars and diffuse sources were removed from the list, so 226 sources remained within  $18'.8$ . In the second step, we corrected the XLF for incompleteness. It is expected that the sensitivity of the detectors is not uniform over the analysed region. To estimate the incompleteness for a flux range, we need to know the fraction of the area, in which the detectors were sensitive enough to de-



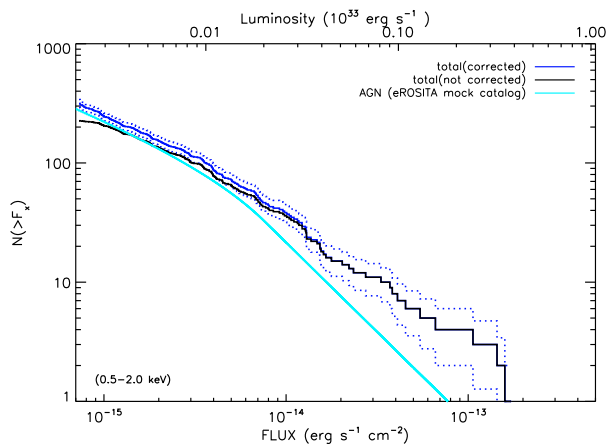


Fig. 11: X-ray luminosity function in the field of 47 Tuc observed by *eROSITA*.

detect a faint source and then correct the number of sources for this incompleteness. For this purpose, we created a sensitivity map of the combined event file of all observations in the energy range of 0.5–2.0 keV using the eSASS task, *apetool*. The sensitivity map gives the detection upper-limits for each pixel of the event file. Using the sensitivity map the cumulative XLF is corrected for incompleteness by the following formula:

$$N(> F_x) = A_{\text{tot}} \sum_{i=1}^{N_s} \frac{1}{\omega(F_i)}, \quad (4)$$

where  $N(> F_x)$  is the number of sources with a flux higher than  $F_x$ . For each source with a flux  $F_i$ , the number is weighted by the normalised effective area  $A_{\text{tot}}/\omega(F_i)$ , where  $A_{\text{tot}}$  is the total area, which have been used to calculate the XLF (i.e., annulus area = 1101.28 arcmin<sup>2</sup>).  $\omega(F_i)$  is the area of pixels, which are sensitive enough to detect sources with a flux  $\geq F_x$ .  $N_s$  is the number of detected sources with a flux above  $\geq F_x$ . In this way the detection of every source is weighted and the XLF gets corrected for the incompleteness.

The XLF includes the members of 47 Tuc and background sources, mainly AGNs. We base the estimation of the number of background AGNs, which should be subtracted from the observed XLF, on the study of [Comparat et al. \(2019\)](#). As [Comparat et al. \(2019\)](#) (their Figure 10) show, the simulation of AGN logN–logS distribution of *eROSITA* in the flux range of  $10^{-16}$  to  $10^{-13}$  erg s<sup>-1</sup> cm<sup>-2</sup> (0.5–2.0 keV) is very well consistent with the results of [Georgakakis et al. \(2008\)](#). Therefore, to obtain the AGN logN–logS distribution for *eROSITA*, we used the broken power-law model suggested by [Georgakakis et al. \(2008\)](#) in the energy range of 0.2–5.0 keV:

$$\frac{dN}{df_x} = \begin{cases} K \left( \frac{f_x}{f_{\text{ref}}} \right)^{\beta_1} & f_x < f_b \\ K' \left( \frac{f_x}{f_{\text{ref}}} \right)^{\beta_2} & f_x \geq f_b, \end{cases} \quad (5)$$

where,  $K' = (f_b/f_{\text{ref}})^{\beta_1 - \beta_2}$ , the break is  $f_b = 10^{-14}$  erg s<sup>-1</sup> cm<sup>-2</sup>,  $K$  is  $1.51 \times 10^{16}$  deg<sup>-2</sup>/erg s<sup>-1</sup> cm<sup>-2</sup>, and  $\beta_1$  and  $\beta_2$  are the power-law indexes for the fluxes lower and higher than the break, –1.58 and –2.50, respectively. The cyan line in the plot (Fig. 11) shows the XLF of AGNs modified for the area of studied region

(0.306 deg<sup>2</sup>) taking into account the Galactic absorption in the direction of 47 Tuc (i.e.,  $5.5 \times 10^{20}$  cm<sup>-2</sup>). The flux of AGNs in the study of [Georgakakis et al. \(2008\)](#) is estimated assuming a power-law model with a photon index of 1.4. To calculate the flux of the sources in the energy range of 0.5–2.0 keV, we assumed the same model. In Fig. 11, the black line shows the observed source distribution, the dark blue line shows the distribution corrected for incompleteness, and the light blue line presents the AGN logN–logS distribution. One can see that there is very small fraction of brighter sources in excess over the background distribution that might belong to 47 Tuc. For low luminosities, no significant excess is observed.

## 6. Summary

In this work we presented the results of analysis of five *eROSITA* observations with the aim of the classification of X-ray sources in the field of this globular cluster. Source detection has been separately performed for five observations of *eROSITA* and 888 sources has been detected in the energy range of 0.2–5.0 keV. Using different methods of X-ray analysis consist of spectral and timing analyses, together with the multi-wavelength studies of the counterparts of X-ray sources in optical, near infrared and infrared surveys, a comprehensive study has been performed for the X-ray sources in the field of 47 Tuc, which resulted to the accurate classification of 15 X-ray sources as members of 47 Tuc. We identified 1 symbiotic stars, 2 quiescent low mass X-ray binaries, and 3 cataclysmic variables. There are 5 sources, which are candidates for either cataclysmic variables or contact binaries and 1 source, which are candidates for RS CVn contact binaries. Moreover, 126 AGNs and background galaxies and 25 Galactic foreground stars are classified in the field of 47 Tuc. We identified 18 sources, which have soft X-ray emission < 0.2 keV and 85 sources, which had hard X-ray emission > 2.0 keV. We could specifically classify one of the foreground stars as an flaring M dwarf based on X-ray variability, spectral analysis, and its infrared/optical counterpart. The XLF of 47 Tuc has been calculated. The result shows that there is no significant sign of population of X-ray sources that belongs to the globular cluster at low luminosities.

*Acknowledgements.* This research was funded by the DLR research grant BWWI/DLR 500R1907. This study is based on observations obtained with *eROSITA*, primary instrument aboard SRG, a joint Russian-German science mission supported by the Russian Space Agency (Roskosmos), in the interests of the Russian Academy of Sciences represented by its Space Research Institute (IKI), and the Deutsches Zentrum für Luft- und Raumfahrt (DLR). The SRG spacecraft was built by Lavochkin Association (NPOL) and its subcontractors, and is operated by NPOL with support from IKI and the Max Planck Institute for Extraterrestrial Physics (MPE). The development and construction of the *eROSITA* X-ray instrument was led by MPE, with contributions from the Dr. Karl Remeis Observatory Bamberg & ECAP (FAU Erlangen-Nürnberg), the University of Hamburg Observatory, the Leibniz Institute for Astrophysics Potsdam (AIP), and the Institute for Astronomy and Astrophysics of the University of Tübingen, with the support of DLR and the Max Planck Society. The *eROSITA* data shown here were processed using the eSASS software system developed by the German *eROSITA* consortium. This research has made use of the SIMBAD and VIZIER database, operated at CDS, Strasbourg, France, and of the NASA/IPAC Extra-galactic Database (NED), which is operated by the Jet Propulsion Laboratory, California Institute of Technology, under contract with the National Aeronautics and Space Administration. This publication makes use of data products from the Wide field Infrared Survey Explorer, which is a joint project of the University of California, Los Angeles, and the Jet Propulsion Laboratory/California Institute of Technology, funded by the National Aeronautics and Space Administration. This publication has made use of data products from the Two Micron All Sky Survey, which is a joint project of the University of Massachusetts and the Infrared Processing and Analysis Center, funded by the National Aeronautics and Space Administration and the National Science Foundation. Funding for SDSS and SDSS-III has been provided by the Alfred P. Sloan Foundation, the Participating Institutions, the National

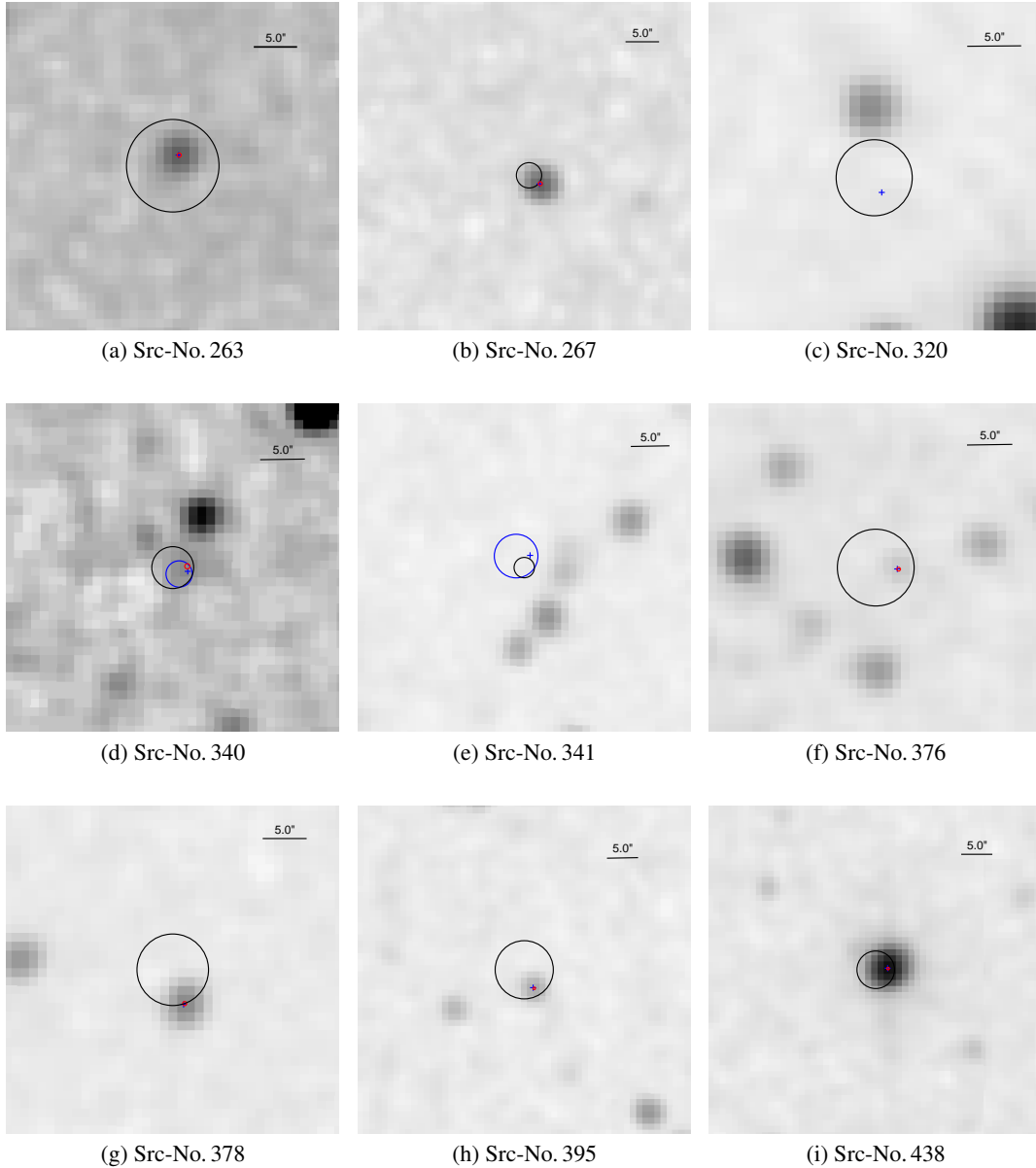
Science Foundation, and the US Department of Energy Office of Science. The SDSS-III web site is <http://www.sdss3.org/>. SDSS-III is managed by the Astrophysical Research Consortium for the Participating Institutions of the SDSS-III Collaboration including the University of Arizona, the Brazilian Participation Group, Brookhaven National Laboratory, University of Cambridge, University of Florida, the French Participation Group, the German Participation Group, the Instituto de Astrofísica de Canarias, the Michigan State/Notre Dame/JINA Participation Group, Johns Hopkins University, Lawrence Berkeley National Laboratory, Max Planck Institute for Astrophysics, New Mexico State University, New York University, Ohio State University, Pennsylvania State University, University of Portsmouth, Princeton University, the Spanish Participation Group, University of Tokyo, University of Utah, Vanderbilt University, University of Virginia, University of Washington, and Yale University. This research has made use of SAO Image DS9, developed by Smithsonian Astrophysical Observatory.

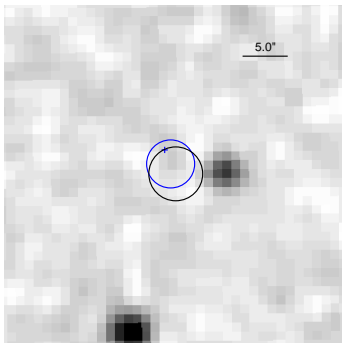
## References

- Akras, S., Leal-Ferreira, M. L., Guzman-Ramirez, L., & Ramos-Larios, G. 2019, *MNRAS*, 483, 5077
- Altamirano, D., Casella, P., Patruno, A., Wijnands, R., & van der Klis, M. 2008, *ApJ*, 674, L45
- Auriere, M., Koch-Miramond, L., & Ortolani, S. 1989, *A&A*, 214, 113
- Bacher, A., Kimeswenger, S., & Teutsch, P. 2005, *MNRAS*, 362, 542
- Bahramian, A., Heinke, C. O., Sivakoff, G. R., et al. 2014, *ApJ*, 780, 127
- Bailer-Jones, C. A. L., Fouesneau, M., & Andrae, R. 2019, *MNRAS*, 490, 5615
- Bailer-Jones, C. A. L., Rybizki, J., Fouesneau, M., Demleitner, M., & Andrae, R. 2021, *VizieR Online Data Catalog*, I/352
- Bailer-Jones, C. A. L., Rybizki, J., Fouesneau, M., Mantelet, G., & Andrae, R. 2018, *AJ*, 156, 58
- Balman, S. 2012, *Mem. Soc. Astron. Italiana*, 83, 585
- Bassa, C., Pooley, D., Homer, L., et al. 2004, *ApJ*, 609, 755
- Bassa, C. G., Pooley, D., Verbunt, F., et al. 2008, *A&A*, 488, 921
- Becker, W. & Trümper, J. 1999, *A&A*, 341, 803
- Belloni, D., Giersz, M., Rivera Sandoval, L. E., Askar, A., & Ciecieląg, P. 2019, *MNRAS*, 483, 315
- Bernardini, F. & Cackett, E. M. 2014, *MNRAS*, 439, 2771
- Bhattacharya, S., Heinke, C. O., Chugunov, A. I., et al. 2017, *MNRAS*, 472, 3706
- Bogdanov, S., Grindlay, J. E., Heinke, C. O., et al. 2006, *ApJ*, 646, 1104
- Brown, E. F., Bildsten, L., & Rutledge, R. E. 1998, *ApJ*, 504, L95
- Brunner, H., Liu, T., Lamer, G., et al. 2021, *arXiv e-prints*, arXiv:2106.14517
- Buccheri, R., Bennett, K., Bignami, G. F., et al. 1983, *A&A*, 128, 245
- Buccheri, R., di Gesu, V., Maccarone, M. C., & Sacco, B. 1988, *A&A*, 201, 194
- Campana, S., Colpi, M., Mereghetti, S., Stella, L., & Tavani, M. 1998, *A&A Rev.*, 8, 279
- Carretta, E., Gratton, R. G., Bragaglia, A., D’Orazi, V., & Lucatello, S. 2013, *A&A*, 550, A34
- Chen, S., Richer, H., Caiazzo, I., & Heyl, J. 2018, *ApJ*, 867, 132
- Cheng, Z., Li, Z., Li, X., Xu, X., & Fang, T. 2019, *ApJ*, 876, 59
- Cheng, Z., Li, Z., Xu, X., et al. 2018, *ApJ*, 869, 52
- Clark, G. W. 1975, *ApJ*, 199, L143
- Cohen, R. E., Hempel, M., Mauro, F., et al. 2015, *AJ*, 150, 176
- Cominsky, L., Forman, W., Jones, C., & Tananbaum, H. 1977, *ApJ*, 211, L9
- Comparat, J., Merloni, A., Salvato, M., et al. 2019, *MNRAS*, 487, 2005
- Cordero, M. J., Pilachowski, C. A., Johnson, C. I., et al. 2014, *ApJ*, 780, 94
- Cutri, R. M. & et al. 2014, *VizieR Online Data Catalog*, II/328
- Cutri, R. M., Skrutskie, M. F., van Dyk, S., et al. 2003, *VizieR Online Data Catalog*, II/246
- Dai, X., Griffin, R. D., Kochanek, C. S., Nugent, J. M., & Bregman, J. N. 2015, *ApJS*, 218, 8
- Dempsey, R. C., Linsky, J. L., Fleming, T. A., & Schmitt, J. H. M. M. 1993a, *ApJS*, 86, 599
- Dempsey, R. C., Linsky, J. L., Fleming, T. A., & Schmitt, J. H. M. M. 1997, *ApJ*, 478, 358
- Dempsey, R. C., Linsky, J. L., Schmitt, J. H. M. M., & Fleming, T. A. 1993b, *ApJ*, 413, 333
- Di Salvo, T. & Sanna, A. 2020, *arXiv e-prints*, arXiv:2010.09005
- Dotter, A., Chaboyer, B., Jevremović, D., et al. 2008, *The Dartmouth Stellar Evolution Database*
- Edelson, R. & Malkan, M. 2012, *ApJ*, 751, 52
- Edmonds, P. D., Gilliland, R. L., Heinke, C. O., & Grindlay, J. E. 2003, *ApJ*, 596, 1177
- Flesch, E. W. 2019, *arXiv e-prints*, arXiv:1912.05614
- Gaia Collaboration. 2020, *VizieR Online Data Catalog*, I/350
- Gaia Collaboration, Brown, A. G. A., Vallenari, A., et al. 2018, *A&A*, 616, A1
- Gendre, B., Barret, D., & Webb, N. 2003, *A&A*, 403, L11
- Georgakakis, A., Nandra, K., Laird, E. S., Aird, J., & Trichas, M. 2008, *MNRAS*, 388, 1205
- Gratton, R., Bragaglia, A., Carretta, E., et al. 2019, *A&A Rev.*, 27, 8
- Gratton, R. G., Lucatello, S., Sollima, A., et al. 2013, *A&A*, 549, A41
- Grindlay, J. E., Heinke, C., Edmonds, P. D., & Murray, S. S. 2001, *Science*, 292, 2290
- Haberl, F., Motch, C., & Zickgraf, F. J. 2002, *A&A*, 387, 201
- Hansen, B. M. S., Kalirai, J. S., Anderson, J., et al. 2013, *Nature*, 500, 51
- Hasinger, G., Johnston, H. M., & Verbunt, F. 1994, *A&A*, 288, 466
- Heinke, C. O., Altamirano, D., Cohn, H. N., et al. 2010, *ApJ*, 714, 894
- Heinke, C. O., Grindlay, J. E., Edmonds, P. D., et al. 2005, *ApJ*, 625, 796
- Heinke, C. O., Grindlay, J. E., Lugger, P. M., et al. 2003, *ApJ*, 598, 501
- Heinke, C. O., Ivanov, M. G., Koch, E. W., et al. 2020, *MNRAS*, 492, 5684
- Hertz, P. & Grindlay, J. E. 1983, *ApJ*, 267, L83
- HI4PI Collaboration, Ben Bekhti, N., Flöer, L., et al. 2016, *A&A*, 594, A116
- Homan, J., van den Berg, M., Heinke, C., et al. 2018, *The Astronomer’s Telegram*, 11598, 1
- Jonker, P. G., Steeghs, D., Chakrabarty, D., & Juett, A. M. 2007, *ApJ*, 665, L147
- Kuulkers, E., Norton, A., Schwope, A., & Warner, B. 2006, *X-rays from cataclysmic variables*, Vol. 39, 421–460
- Lane, R. R., Kiss, L. L., Lewis, G. F., et al. 2011, *A&A*, 530, A31
- Luna, G. J. M., Sokoloski, J. L., Mukai, K., & Nelson, T. 2013, *A&A*, 559, A6
- Maccacaro, T., Gioia, I. M., Wolter, A., Zamorani, G., & Stocke, J. T. 1988, *ApJ*, 326, 680
- Marks, M. & Kroupa, P. 2010, *MNRAS*, 406, 2000
- Marocco, F., Eisenhardt, P. R. M., Fowler, J. W., et al. 2021, *ApJS*, 253, 8
- McDonald, I., Boyer, M. L., van Loon, J. T., et al. 2011, *ApJS*, 193, 23
- Mereghetti, S., Kuiper, L., Tiengo, A., et al. 2016, *ApJ*, 831, 21
- Merloni, A., Predehl, P., Becker, W., et al. 2012, *arXiv e-prints*, arXiv:1209.3114
- Monroe, T. R., Prochaska, J. X., Tejos, N., et al. 2016, *AJ*, 152, 25
- Mukai, K. 2017, *PASP*, 129, 062001
- Narloch, W., Kaluzny, J., Poleski, R., et al. 2017, *MNRAS*, 471, 1446
- Paresce, F., de Marchi, G., & Ferraro, F. R. 1992, *Nature*, 360, 46
- Pooley, D., Lewin, W. H. G., Anderson, S. F., et al. 2003, *ApJ*, 591, L131
- Predehl, P., Andritschke, R., Arefiev, V., et al. 2021, *A&A*, 647, A1
- Primini, F. A., Forman, W., & Jones, C. 1993, *ApJ*, 410, 615
- Ramsay, G., Cropper, M., Wu, K., et al. 2004, *MNRAS*, 350, 1373
- Rengarajan, T. N. & Verma, R. P. 1983, *MNRAS*, 205, 447
- Ridolfi, A., Freire, P. C. C., Torne, P., et al. 2016, *MNRAS*, 462, 2918
- Rutledge, R. E., Bildsten, L., Brown, E. F., Pavlov, G. G., & Zavlin, V. E. 2002, *ApJ*, 578, 405
- Salvato, M., Buchner, J., Budavári, T., et al. 2018, *MNRAS*, 473, 4937
- Sanna, A., Bahramian, A., Bozzo, E., et al. 2018, *A&A*, 610, L2
- Sanna, A., Papitto, A., Burderi, L., et al. 2017, *A&A*, 598, A34
- Scargle, J. D. 1982, *ApJ*, 263, 835
- Schlaflly, E. F. & Finkbeiner, D. P. 2011, *ApJ*, 737, 103
- Secrest, N. J., Dudik, R. P., Dorland, B. N., et al. 2015, *ApJS*, 221, 12
- Smith, R. K., Brickhouse, N. S., Liedahl, D. A., & Raymond, J. C. 2001, *ApJ*, 556, L91
- Soszyński, I., Udalski, A., Szymański, M. K., et al. 2011, *Acta Astron.*, 61, 217
- Suleimanov, V. F., Doroshenko, V., & Werner, K. 2019, *MNRAS*, 482, 3622
- van Teeseling, A., Beuermann, K., & Verbunt, F. 1996, *A&A*, 315, 467
- Verbunt, F. & Hasinger, G. 1998, *A&A*, 336, 895
- Wenger, M., Ochsenein, F., Egret, D., et al. 2000, *A&AS*, 143, 9
- West, A. A., Morgan, D. P., Bochanski, J. J., et al. 2011, *AJ*, 141, 97
- Wijnands, R., Heinke, C. O., Pooley, D., et al. 2005, *ApJ*, 618, 883
- Wolf, C., Onken, C. A., Luvaul, L. C., et al. 2018, *PASA*, 35, e010
- Worpel, H., Schwope, A. D., Granzer, T., et al. 2016, *A&A*, 592, A114
- Wright, E. L., Eisenhardt, P. R. M., Mainzer, A. K., et al. 2010, *AJ*, 140, 1868
- Yokogawa, J., Paul, B., Ozaki, M., et al. 2000, *ApJ*, 539, 191
- Zavlin, V. E., Pavlov, G. G., & Shibanov, Y. A. 1996, *A&A*, 315, 141

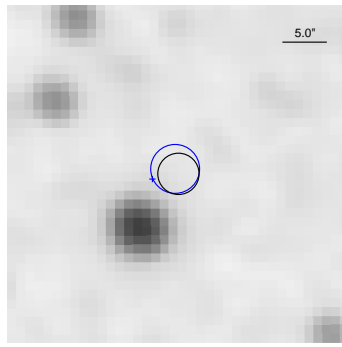
**Appendix A: Image of infrared 2MASS counterparts of 47 Tuc members**

The Infrared 2MASS ( $k_s$  band) images of the X-ray sources, which are classified as members of 47 Tuc (see Sect.5). Images show  $2\sigma$  positional error of *eROSITA* X-ray sources (black). If a source has a *Chandra* counterpart,  $2\sigma$  *Chandra* positional error is shown with blue circle. Infrared 2MASS counterpart is in red circles and blue crosses show the position of optical Gaia counterpart. Since the typical  $3\sigma$  positional error of Gaia counterparts ( $\sim 0.03''$ ) is negligible in comparison to the X-ray and infrared positional errors ( $\sim 0.3''$ ) therefore, they are shown by crosses. The scale of  $5.0''$  is shown for all images.

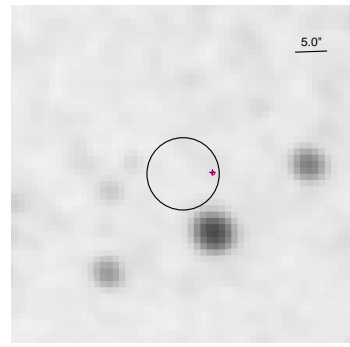




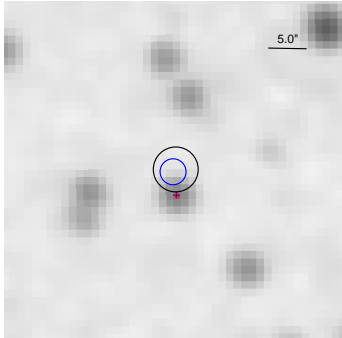
(a) Src-No. 480



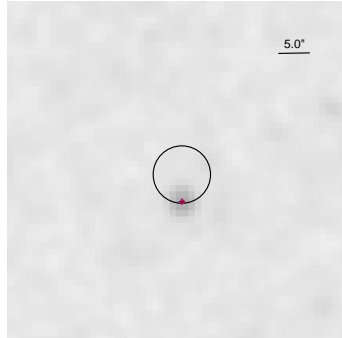
(b) Src-No. 481



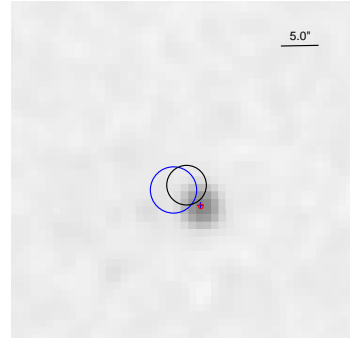
(c) Src-No. 486



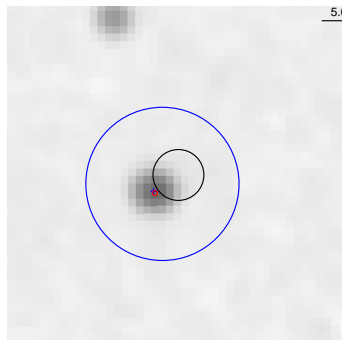
(d) Src-No. 501



(e) Src-No. 522



(f) Src-No. 552



(g) Src-No. 556



Table B.1: X-ray sources in the FOV of 47 Tuc.<sup>†</sup>:

NO	eROSITA SRC-Name	RA (J2000)	DEC (J2000)	r1 $\sigma$ (")	Flux (0.2–5. keV) (10 <sup>-14</sup> erg s <sup>-1</sup> cm <sup>-2</sup> )				Hardness ratio			Var	Classification*	CATA**		
					OBS1	OBS2	OBS3	OBS4	OBS5	HR1	HR2				HR3	
1	SRGJ001544.20-720140.6	00 15 44.20	-72 01 40.6	4.76	–	3.55± 0.93	–	–	–	–	0.26± 0.46	0.26± 0.27	-0.11± 0.31	–		
2	SRGJ001548.65-720510.1	00 15 48.65	-72 05 10.1	2.53	–	5.13± 0.90	–	–	–	–	0.57± 0.25	0.22± 0.14	-0.73± 0.24	–	CalPV	
3	SRGJ001551.31-715137.4	00 15 51.31	-71 51 37.4	5.55	–	3.11± 0.87	–	–	–	–	-0.17± 0.24	-0.24± 0.32	-0.19± 0.63	–		
4	SRGJ001557.06-714549.5	00 15 57.06	-71 45 49.5	3.35	–	2.47± 0.83	–	–	–	–	1.00± 5.69	-1.00± 12.52	1.00± 0.23	–		
5	SRGJ001603.49-720731.1	00 16 03.49	-72 07 31.1	3.35	–	28.56± 4.54	–	–	–	–	-0.13± 0.19	0.06± 0.19	0.01± 0.22	–		
6	SRGJ001604.75-715457.3	00 16 04.75	-71 54 57.3	4.59	–	2.93± 0.77	–	–	–	–	-0.51± 0.24	0.04± 0.39	-0.04± 0.49	–		
7	SRGJ001612.87-715258.7	00 16 12.87	-71 52 58.7	2.22	–	4.87± 0.82	–	–	–	–	0.31± 0.17	-0.38± 0.16	-0.27± 0.34	–	CalPV	
8	SRGJ001614.22-715703.0	00 16 14.22	-71 57 03.0	4.17	–	3.27± 0.80	–	–	–	–	-0.39± 0.36	-1.00± 1.12	1.00± 0.31	–		
9	SRGJ001614.84-720047.6	00 16 14.84	-72 00 47.6	3.35	–	32.48± 5.56	–	–	–	–	0.07± 0.19	0.05± 0.17	-0.42± 0.28	–	CalPV	
10	SRGJ001623.31-714300.9	00 16 23.31	-71 43 00.9	3.35	–	9.17± 2.50	–	–	–	–	–	–	1.00± 0.32	–		
11	SRGJ001623.93-721837.7	00 16 23.93	-72 18 37.7	3.44	–	–	–	–	36.34± 6.85	0.10± 0.29	0.51± 0.14	-0.73± 0.26	–	–		
12	SRGJ001624.39-715206.3	00 16 24.39	-71 52 06.3	2.52	–	5.52± 0.83	–	–	–	0.39± 0.22	0.09± 0.15	-0.37± 0.20	–	–	AGN	
13	SRGJ001628.21-714710.1	00 16 28.21	-71 47 10.1	3.35	–	62.70± 7.86	–	–	–	–	-0.01± 0.17	0.30± 0.13	-0.65± 0.17	–	CalPV	
14	SRGJ001631.67-715352.0	00 16 31.67	-71 53 52.0	3.35	–	3.30± 0.70	–	–	–	–	-0.05± 0.23	-0.14± 0.24	-0.21± 0.37	–	CalPV	
15	SRGJ001635.62-715229.2	00 16 35.62	-71 52 29.2	2.32	–	1.58± 0.31	–	–	–	–	-0.17± 0.26	0.26± 0.22	-1.00± 0.11	–	CalPV	
16	SRGJ001633.64-721027.9	00 16 33.64	-72 10 27.9	3.44	–	–	–	–	16.67± 1.84	0.01± 0.17	0.35± 0.12	-0.15± 0.13	–	–	CalPV	
17	SRGJ001636.75-721030.2	00 16 36.75	-72 10 30.2	3.35	–	40.91± 4.25	–	–	–	0.23± 0.13	0.08± 0.10	-0.41± 0.15	–	–		
18	SRGJ001637.21-715815.7	00 16 37.21	-71 58 15.7	3.35	–	22.39± 2.87	–	–	–	0.05± 0.14	0.02± 0.12	-0.59± 0.23	–	–	CalPV	
19	SRGJ001641.90-720456.7	00 16 41.90	-72 04 56.7	3.44	–	2.62± 0.52	–	–	3.63± 0.77	0.40± 0.21	-0.37± 0.21	-0.40± 0.44	1.38± 0.41	–	CalPV	
20	SRGJ001643.69-720643.4	00 16 43.69	-72 06 43.4	3.27	–	–	–	–	4.53± 1.10	-0.36± 0.24	-0.28± 0.45	0.58± 0.32	–	–		
21	SRGJ001642.52-714751.5	00 16 42.52	-71 47 51.5	3.30	–	4.77± 0.82	–	–	–	0.34± 0.18	-0.21± 0.16	-1.00± 0.34	–	–	CalPV	
22	SRGJ001646.63-715202.0	00 16 46.63	-71 52 02.0	3.35	–	32.36± 3.51	–	–	–	0.24± 0.11	-0.30± 0.11	-0.47± 0.22	–	–	CalPV	
23	SRGJ001649.65-713915.3	00 16 49.65	-71 39 15.3	3.69	–	2.28± 0.63	–	–	–	–	–	1.00± 0.18	–	–		
24	SRGJ001655.56-721639.3	00 16 55.56	-72 16 39.3	4.68	–	3.95± 0.93	–	–	–	-0.41± 0.22	0.11± 0.30	-0.39± 0.46	–	–		
25	SRGJ001657.89-720327.1	00 16 57.89	-72 03 27.1	3.13	–	1.98± 0.48	–	–	5.81± 0.92	0.22± 0.19	-0.30± 0.19	0.20± 0.23	–	–	CalPV	
26	SRGJ001656.20-714056.6	00 16 56.20	-71 40 56.6	4.61	–	12.82± 1.56	–	–	–	-0.12± 0.12	0.05± 0.12	-0.54± 0.23	–	–	CalPV	
27	SRGJ001659.42-722112.6	00 16 59.42	-72 21 12.6	3.44	–	–	–	–	2.53± 0.72	-0.22± 0.29	0.32± 0.26	-1.00± 0.56	–	–		
28	SRGJ001700.81-714510.4	00 17 00.81	-71 45 10.4	3.97	–	2.51± 0.62	–	–	–	0.02± 0.23	-0.24± 0.27	-1.00± 0.63	–	–	CalPV	
29	SRGJ001701.85-714327.2	00 17 01.85	-71 43 27.2	3.35	–	11.46± 2.25	–	–	–	0.01± 0.30	0.30± 0.20	-0.13± 0.24	–	–		
30	SRGJ001702.05-715038.5	00 17 02.05	-71 50 38.5	2.85	–	3.75± 0.72	–	–	–	0.04± 0.22	-0.06± 0.22	-0.22± 0.31	–	–	CalPV	
31	SRGJ001702.84-714153.8	00 17 02.84	-71 41 53.8	4.38	–	3.57± 0.92	–	–	–	0.28± 0.29	-0.32± 0.28	0.05± 0.41	–	–	CalPV	
32	SRGJ001705.00-720059.1	00 17 05.00	-72 00 59.1	3.44	–	2.14± 0.60	–	–	20.47± 3.16	-0.24± 0.19	0.19± 0.20	0.11± 0.20	9.56± 0.44	–	CalPV	
33	SRGJ001703.32-721816.4	00 17 03.32	-72 18 16.4	4.54	–	3.02± 0.89	–	–	–	-1.00± 0.22	1.00± 1.06	-0.08± 0.67	–	–		
34	SRGJ001704.34-722518.4	00 17 04.34	-72 25 18.4	3.44	–	–	–	–	25.07± 4.06	0.02± 0.20	0.11± 0.17	-0.13± 0.22	–	–		
35	SRGJ001707.68-713856.7	00 17 07.68	-71 38 56.7	1.78	–	12.19± 1.12	–	–	–	0.31± 0.11	0.01± 0.09	-0.55± 0.13	–	–	AGN	
36	SRGJ001711.60-715657.9	00 17 11.60	-71 56 57.9	3.44	–	–	–	–	3.64± 1.02	–	–	1.00± 0.07	–	–		
37	SRGJ001715.21-721741.1	00 17 15.21	-72 17 41.1	3.91	–	3.74± 0.90	–	–	–	-0.21± 0.29	0.24± 0.27	-0.21± 0.33	–	–		
38	SRGJ001714.44-720352.9	00 17 14.44	-72 03 52.9	2.58	–	4.35± 0.65	–	–	5.29± 0.73	0.38± 0.18	0.16± 0.12	-1.00± 0.18	–	–	CalPV	
39	SRGJ001716.31-715750.7	00 17 16.31	-71 57 50.7	1.80	–	2.99± 0.55	–	–	11.83± 1.97	0.31± 0.25	0.01± 0.19	-0.04± 0.21	3.95± 0.35	–	AGN	
40	SRGJ001721.18-721313.7	00 17 21.18	-72 13 13.7	3.57	–	–	–	–	2.40± 0.63	0.71± 1.17	0.58± 0.26	-0.17± 0.26	–	–		
41	SRGJ001721.35-715454.2	00 17 21.35	-71 54 54.2	1.51	–	5.13± 0.63	–	–	3.70± 0.54	0.38± 0.11	-0.52± 0.12	-0.58± 0.34	–	–	FG	
42	SRGJ001722.04-720527.8	00 17 22.04	-72 05 27.8	3.44	–	–	–	–	17.32± 3.11	0.74± 0.25	-0.35± 0.17	0.11± 0.25	–	–		
43	SRGJ001722.11-713803.8	00 17 22.11	-71 38 03.8	4.68	–	4.06± 0.97	–	–	–	0.14± 0.38	0.12± 0.28	0.05± 0.29	–	–		
44	SRGJ001725.02-720554.6	00 17 25.02	-72 05 54.6	3.54	–	1.98± 0.51	–	–	–	0.11± 0.34	0.33± 0.22	-1.00± 0.37	–	–	CalPV	
45	SRGJ001726.27-715028.9	00 17 26.27	-71 50 28.9	3.35	–	173.69± 2.63	–	–	–	0.22± 0.02	-0.08± 0.02	-0.80± 0.02	–	–	AGN	
46	SRGJ001732.21-720357.3	00 17 32.21	-72 03 57.3	2.07	–	3.04± 0.56	–	–	1.76± 0.47	0.81± 0.49	-0.01± 0.23	-1.00± 0.17	1.73± 0.45	–	AGN	
47	SRGJ001732.67-721137.2	00 17 32.67	-72 11 37.2	2.90	–	2.11± 0.62	–	–	2.15± 0.49	0.38± 0.31	0.14± 0.20	-1.00± 0.30	1.02± 0.52	–	CalPV	
48	SRGJ001737.03-722611.0	00 17 37.03	-72 26 11.0	2.00	–	–	–	–	8.32± 0.94	-0.06± 0.13	0.09± 0.12	-0.46± 0.18	–	–	AGN	

<sup>†</sup>: Full catalogue is available online.

\*: AB: active binary; AGN: Active galactic nuclei; CV: Cataclysmic variable; FG: Foreground star; SYM: Symbiotic star; QLMXB: Quiescent LMXB.

\*\*\*: Source is in the eROSITA CalPV catalogue as well.

Table B.2: Infrared magnitudes of counterparts of X-ray sources of 47 Tuc in different energy filters 2MASS and WISE surveys.†

No	W1 mag	W2 mag	W3 mag	W4 mag	J mag	H mag	K <sub>s</sub> mag
3	18.02± 0.19	17.10± 0.31	< 12.94	< 9.10	–	–	–
4	14.57± 0.03	14.62± 0.05	< 12.72	< 9.31	15.15± 0.05	14.72± 0.08	14.71± 0.08
5	17.20± 0.10	16.86± 0.24	< 12.20	< 8.58	–	–	–
6	17.32± 0.10	17.04± 0.29	< 13.08	< 8.85	–	–	–
9	16.29± 0.05	15.98± 0.12	< 12.21	< 9.02	–	–	–
10	16.63± 0.07	16.52± 0.19	< 12.71	< 9.39	–	–	–
11	16.68± 0.06	16.12± 0.12	< 12.55	< 9.05	–	–	–
12	14.02± 0.03	13.75± 0.03	< 12.17	< 9.48	16.00± 0.10	15.43± 0.13	14.60± 0.13
13	17.44± 0.12	17.27± 0.36	< 12.94	< 8.72	–	–	–
14	17.11± 0.09	17.32± 0.37	< 12.87	< 9.19	–	–	–
16	17.00± 0.08	17.07± 0.29	< 12.79	< 9.11	–	–	–
21	17.60± 0.13	16.80± 0.23	< 12.54	< 9.19	–	–	–
22	16.88± 0.08	15.88± 0.10	< 12.53	< 8.76	–	–	–
23	17.02± 0.08	16.53± 0.18	< 12.92	< 9.27	–	–	–
24	16.78± 0.07	16.56± 0.18	< 12.41	< 9.37	–	–	–
25	17.05± 0.09	17.07± 0.29	< 12.37	< 9.26	–	–	–
26	16.92± 0.08	16.01± 0.11	< 12.82	< 9.28	–	–	–
28	16.14± 0.05	15.71± 0.09	< 12.56	< 9.09	–	–	–
29	18.13± 0.21	17.22± 0.33	< 13.01	< 8.99	–	–	–
30	11.91± 0.02	11.99± 0.02	11.87± 0.19	< 9.45	12.64± 0.02	12.07± 0.03	11.99± 0.03
31	17.36± 0.11	16.49± 0.17	< 12.65	< 8.97	–	–	–
32	16.93± 0.08	17.35± 0.39	< 12.32	< 8.94	–	–	–
33	15.02± 0.03	15.14± 0.06	< 12.77	< 8.74	15.69± 0.07	15.20± 0.10	15.08± 0.10
35	15.33± 0.03	14.26± 0.04	11.59± 0.17	9.12± 0.42	–	–	–
36	16.79± 0.07	16.91± 0.25	< 13.12	< 9.09	–	–	–
37	17.00± 0.08	17.11± 0.30	< 12.99	< 8.71	–	–	–
38	16.66± 0.07	15.75± 0.10	< 12.33	< 8.71	–	–	–
39	15.33± 0.03	15.08± 0.06	12.93± 0.52	< 9.31	–	–	–
40	16.15± 0.05	16.08± 0.12	< 12.73	< 9.17	–	–	–
41	9.10± 0.02	9.11± 0.02	9.05± 0.03	9.08± 0.41	9.35± 0.02	9.19± 0.02	9.13± 0.02
42	15.30± 0.03	15.38± 0.07	< 12.55	< 8.88	15.95± 0.08	15.39± 0.11	15.13± 0.11
44	17.27± 0.10	16.99± 0.28	12.41± 0.32	< 8.75	–	–	–
45	12.04± 0.02	11.39± 0.02	8.84± 0.02	6.61± 0.05	14.72± 0.06	13.81± 0.06	13.26± 0.06
46	16.65± 0.06	15.34± 0.07	11.69± 0.18	< 9.20	–	–	–
48	16.01± 0.04	15.09± 0.06	12.41± 0.34	< 9.25	–	–	–
49	16.84± 0.08	16.22± 0.14	< 12.38	< 8.89	–	–	–
50	15.53± 0.04	15.51± 0.08	< 12.99	< 9.29	15.92± 0.08	15.70± 0.14	15.64± 0.14
51	16.08± 0.05	15.28± 0.07	< 12.15	< 8.79	–	–	–
54	18.12± 0.22	16.67± 0.20	< 12.67	< 8.89	–	–	–
55	16.57± 0.06	16.64± 0.20	13.01± 0.52	< 8.67	–	–	–
56	15.43± 0.03	15.15± 0.06	12.56± 0.40	< 9.27	–	–	–
60	13.62± 0.03	13.39± 0.03	12.45± 0.41	< 8.63	15.60± 0.09	14.81± 0.09	14.23± 0.09
61	16.45± 0.06	16.38± 0.16	< 12.23	< 9.12	–	–	–
62	16.38± 0.05	15.03± 0.06	11.60± 0.15	9.22± 0.50	–	–	–
63	14.70± 0.03	14.27± 0.04	12.05± 0.25	9.00± 0.39	–	–	–
66	15.16± 0.03	14.47± 0.04	11.16± 0.13	9.18± 0.52	–	–	–
68	17.15± 0.09	16.00± 0.11	< 12.14	< 8.92	–	–	–
69	16.21± 0.05	15.05± 0.06	11.63± 0.16	8.97± 0.42	–	–	–
70	17.65± 0.14	16.53± 0.18	< 12.98	< 9.18	–	–	–
.							
.							
.							

---

†: Full catalogue is available online.

Table B.3: Optical magnitudes of counterparts of X-ray sources of 47 Tuc in Gaia and SkyMapper Southern Sky Survey.

NO	Gaia magnitudes(Gaia Collaboration 2020)			SkyMapper magnitudes(Wolf et al. 2018)		Gaia distance (Bailer-Jones et al. 2018) pc
	G mag 300 nm	G <sub>BP</sub> mag 400-500 nm	G <sub>RP</sub> mag 600-750 nm	g mag 467 nm	r mag 616 nm	
4	16.331± 0.001	16.698± 0.004	15.767± 0.003	–	–	
9	17.392± 0.001	17.728± 0.008	16.882± 0.009	–	–	
30	13.912± 0.000	14.366± 0.001	13.296± 0.001	–	–	
33	17.319± 0.001	17.870± 0.010	16.621± 0.006	–	–	
41	10.024± 0.010	10.252± 0.030	9.714± 0.030	10.382± 0.003	10.274± 0.003	361.985± 2.893
45	17.207± 0.006	16.986± 0.017	15.938± 0.010	–	–	
50	17.067± 0.001	17.392± 0.007	16.558± 0.006	17.640± 0.086	17.061± 0.056	
71	9.792± 0.001	10.081± 0.002	9.373± 0.001	–	–	160.834± 2.976
81	17.103± 0.001	17.405± 0.013	16.597± 0.009	–	–	
84	15.640± 0.002	17.442± 0.012	14.308± 0.002	–	–	66.503± 1.648
106	17.331± 0.001	17.642± 0.010	16.847± 0.009	–	–	
109	16.871± 0.001	17.558± 0.010	16.067± 0.002	–	–	
119	16.579± 0.001	17.077± 0.006	15.934± 0.003	16.921± 0.089	16.563± 0.078	
137	16.713± 0.001	17.125± 0.005	16.111± 0.005	–	–	
145	16.376± 0.001	16.661± 0.005	15.924± 0.005	16.719± 0.136	16.494± 0.031	
148	13.100± 0.003	13.912± 0.003	12.212± 0.004	13.944± 0.010	13.214± 0.007	149.648± -0.621
158	17.585± 0.001	17.909± 0.012	17.119± 0.010	17.848± 0.130	17.622± 0.146	
161	17.069± 0.001	17.455± 0.010	16.509± 0.006	17.493± 0.142	17.244± 0.115	
162	21.120± 0.024	–	–	–	–	
164	21.100± 0.025	–	–	17.210± 0.211	17.050± 0.116	
181	17.164± 0.001	17.491± 0.013	16.674± 0.005	17.346± 0.197	17.277± 0.091	
192	12.158± 0.000	12.665± 0.002	11.521± 0.001	12.603± 0.004	12.155± 0.004	162.665± -0.779
215	16.706± 0.003	17.988± 0.012	15.498± 0.005	–	–	297.176± 29.835
217	17.215± 0.001	17.873± 0.012	16.430± 0.004	–	–	
218	16.411± 0.001	17.196± 0.008	15.556± 0.003	–	–	668.550± 26.177
220	17.206± 0.001	17.506± 0.010	16.707± 0.008	17.395± 0.165	17.409± 0.075	
232	17.783± 0.001	17.959± 0.026	17.172± 0.013	–	–	
246	16.637± 0.001	17.072± 0.005	16.042± 0.004	16.864± 0.099	16.486± 0.075	
247	17.005± 0.001	17.360± 0.015	16.490± 0.006	17.354± 0.113	17.267± 0.134	
255	15.024± 0.001	16.126± 0.007	13.979± 0.002	16.363± 0.030	15.333± 0.019	168.927± 0.872
260	17.113± 0.003	17.765± 0.016	16.333± 0.009	–	–	999.932± 81.000
262	17.057± 0.001	17.393± 0.011	16.549± 0.011	–	–	
263	14.771± 0.000	15.269± 0.003	14.109± 0.002	15.247± 0.023	14.801± 0.016	
267	13.379± 0.000	13.845± 0.002	12.761± 0.001	13.794± 0.009	13.411± 0.008	
279	17.677± 0.001	17.939± 0.017	17.160± 0.012	–	–	
282	17.556± 0.001	17.702± 0.023	16.951± 0.024	17.292± 0.124	16.775± 0.106	
285	17.544± 0.001	17.861± 0.013	17.078± 0.008	18.143± 0.219	17.846± 0.114	
304	11.561± 0.000	11.796± 0.002	11.186± 0.001	–	–	402.812± 3.975
313	12.016± 0.000	12.688± 0.001	11.250± 0.001	–	–	
330	17.652± 0.001	17.878± 0.013	17.098± 0.013	17.351± 0.165	17.600± 0.208	
332	13.862± 0.000	14.318± 0.001	13.255± 0.001	14.239± 0.011	13.915± 0.009	
335	17.127± 0.002	17.141± 0.029	16.276± 0.044	14.111± 0.013	13.799± 0.010	
337	16.924± 0.001	17.322± 0.010	16.365± 0.006	–	–	
340	17.416± 0.002	17.190± 0.044	16.370± 0.028	16.831± 0.113	16.350± 0.076	
341	17.342± 0.003	17.514± 0.011	16.705± 0.010	–	–	
355	17.835± 0.002	17.895± 0.020	17.067± 0.024	–	–	
359	16.385± 0.001	16.700± 0.004	15.899± 0.004	–	–	
361	17.430± 0.002	17.351± 0.024	16.492± 0.035	16.894± 0.100	16.713± 0.070	
364	19.071± 0.004	–	–	16.912± 0.148	16.314± 0.092	
365	17.360± 0.001	17.641± 0.009	16.856± 0.008	–	–	
369	17.115± 0.001	17.397± 0.012	16.582± 0.010	17.370± 0.162	17.433± 0.178	
371	17.786± 0.002	17.730± 0.047	17.011± 0.030	14.240± 0.013	13.876± 0.010	
374	17.616± 0.002	17.193± 0.053	16.466± 0.034	–	–	
376	15.857± 0.003	16.155± 0.007	15.128± 0.005	14.669± 0.017	14.269± 0.013	
378	13.862± 0.000	14.405± 0.002	13.184± 0.000	–	–	
384	17.617± 0.001	17.619± 0.010	17.928± 0.008	–	–	
385	17.376± 0.001	17.952± 0.016	16.606± 0.012	–	–	
389	18.655± 0.013	17.749± 0.032	16.636± 0.009	16.307± 0.110	16.021± 0.096	
394	17.737± 0.007	17.548± 0.019	16.453± 0.012	16.896± 0.151	17.044± 0.182	
395	14.703± 0.003	15.081± 0.007	13.965± 0.005	14.839± 0.023	14.483± 0.017	
396	15.941± 0.001	16.799± 0.005	15.039± 0.003	16.882± 0.081	16.028± 0.022	
402	17.544± 0.001	17.619± 0.021	16.648± 0.033	16.281± 0.082	16.658± 0.632	
403	18.405± 0.006	17.784± 0.039	16.882± 0.024	–	–	
422	20.944± 0.036	–	–	17.917± 0.305	17.228± 0.223	

Continued on the next page

Continued from previous page

NO	Gaia magnitudes(Gaia Collaboration 2020)			SkyMapper magnitudes (Wolf et al. 2018)		Gaia distance (Bailer-Jones et al. 2018) pc
	G mag	G <sub>BP</sub> mag	G <sub>RP</sub> mag	g mag	r mag	
	300 nm	400-500 nm	600-750 nm	353-358 nm	379-384 nm	
424	14.341± 0.001	15.531± 0.006	13.223± 0.002	–	–	85.457± 0.238
427	17.094± 0.001	17.429± 0.012	16.606± 0.006	–	–	
428	9.960± 0.000	10.324± 0.002	9.438± 0.004	–	–	128.468± 0.578
435	9.390± 0.010	9.007± 0.003	8.395± 0.004	9.065± 0.003	8.994± 0.003	
438	11.053± 0.001	11.963± 0.002	10.148± 0.001	11.995± 0.003	11.183± 0.003	
443	21.069± 0.030	–	–	–	–	
449	8.876± 0.000	9.290± 0.001	8.332± 0.002	9.284± 0.003	9.065± 0.003	53.144± 0.320
453	16.377± 0.003	17.696± 0.020	15.196± 0.006	–	–	200.460± -4.190
456	16.671± 0.001	17.106± 0.010	16.067± 0.004	16.930± 0.138	16.759± 0.050	
463	17.024± 0.003	17.153± 0.011	16.273± 0.007	17.650± 0.220	17.538± 0.198	
465	17.345± 0.001	17.372± 0.021	16.622± 0.017	14.152± 0.012	13.695± 0.009	
471	17.757± 0.006	17.315± 0.048	16.624± 0.023	14.829± 0.020	14.324± 0.014	
472	11.512± 0.001	11.910± 0.002	10.975± 0.002	11.826± 0.003	11.499± 0.003	649.205± 8.735
481	17.620± 0.003	17.687± 0.031	16.841± 0.036	–	–	
486	17.191± 0.002	17.321± 0.010	16.514± 0.010	0.000± 0.005	0.000± 0.004	
495	17.326± 0.001	17.603± 0.009	16.814± 0.009	17.965± 0.282	17.188± 0.086	
496	13.073± 0.000	13.530± 0.002	12.468± 0.001	–	–	
501	13.639± 0.000	14.191± 0.002	12.936± 0.001	14.214± 0.013	13.699± 0.009	
502	17.026± 0.001	17.373± 0.008	16.497± 0.006	–	–	
515	21.147± 0.029	–	–	–	–	
522	14.760± 0.000	15.249± 0.002	14.113± 0.002	15.196± 0.024	14.828± 0.018	
549	17.343± 0.001	17.654± 0.010	16.876± 0.008	–	–	
550	15.087± 0.001	16.487± 0.004	13.922± 0.002	–	–	152.539± 0.785
556	12.804± 0.000	13.395± 0.002	12.090± 0.001	13.347± 0.007	12.825± 0.004	
558	17.838± 0.005	17.785± 0.021	17.013± 0.013	17.911± 0.297	17.716± 0.099	
575	14.036± 0.002	14.469± 0.006	13.439± 0.006	–	–	
580	12.292± 0.000	12.662± 0.001	11.765± 0.002	–	–	
589	17.521± 0.001	17.839± 0.013	17.037± 0.008	–	–	
591	17.705± 0.002	17.682± 0.043	16.749± 0.034	17.587± 0.168	17.094± 0.112	
593	17.563± 0.001	17.867± 0.016	17.088± 0.006	17.830± 0.135	17.622± 0.126	
596	17.560± 0.001	17.855± 0.013	17.086± 0.013	–	–	
599	17.226± 0.001	17.867± 0.008	16.468± 0.005	–	–	
604	12.388± 0.002	12.794± 0.005	11.837± 0.004	12.827± 0.005	12.505± 0.004	531.254± 7.155
609	16.884± 0.001	17.280± 0.007	16.315± 0.003	17.295± 0.132	17.056± 0.104	
632	19.182± 0.021	–	–	–	13.185± 0.015	
635	16.282± 0.001	17.003± 0.007	15.472± 0.003	–	–	
641	16.154± 0.001	16.597± 0.004	15.555± 0.002	–	–	
650	19.006± 0.011	–	–	16.053± 0.095	16.075± 0.120	
693	16.326± 0.003	17.167± 0.009	14.446± 0.008	17.249± 0.085	16.126± 0.043	125.354± 6.518
702	15.099± 0.001	15.737± 0.003	14.335± 0.002	15.767± 0.034	15.142± 0.042	441.093± 5.280
713	16.750± 0.001	17.310± 0.009	16.037± 0.003	17.244± 0.136	16.955± 0.097	
715	17.246± 0.001	17.552± 0.015	16.740± 0.008	–	–	
720	20.180± 0.010	–	–	–	–	
722	15.461± 0.001	15.923± 0.003	14.832± 0.002	–	–	
725	16.735± 0.001	17.408± 0.006	15.951± 0.003	17.458± 0.174	16.876± 0.100	
729	16.857± 0.001	17.163± 0.008	16.368± 0.007	17.102± 0.121	16.810± 0.047	
738	14.278± 0.000	14.803± 0.002	13.614± 0.001	14.785± 0.016	14.304± 0.008	
743	14.905± 0.000	15.295± 0.002	14.364± 0.002	15.212± 0.024	14.980± 0.019	
744	15.821± 0.001	16.876± 0.007	14.797± 0.002	–	–	400.311± 5.762
758	16.646± 0.001	17.361± 0.008	15.832± 0.003	17.380± 0.159	16.681± 0.053	
763	16.956± 0.001	17.633± 0.010	16.171± 0.006	17.914± 0.091	16.894± 0.048	
804	17.517± 0.001	17.795± 0.023	17.022± 0.010	–	–	
820	11.403± 0.001	12.040± 0.004	10.663± 0.003	12.081± 0.003	11.501± 0.003	
828	17.031± 0.001	17.369± 0.011	16.506± 0.006	–	–	
829	17.667± 0.001	17.965± 0.017	17.183± 0.009	–	–	
836	13.596± 0.000	13.887± 0.001	13.148± 0.001	13.826± 0.005	13.605± 0.006	727.419± 8.424
851	16.702± 0.001	17.454± 0.013	15.862± 0.004	17.377± 0.139	16.868± 0.083	
852	13.222± 0.000	14.050± 0.003	12.337± 0.001	10.285± 0.003	10.072± 0.003	122.876± 0.267
864	9.341± 0.000	9.552± 0.001	9.030± 0.002	9.523± 0.003	9.496± 0.003	272.845± 1.717
873	12.051± 0.001	12.540± 0.004	11.436± 0.003	12.508± 0.004	12.073± 0.004	697.843± 11.248
888	17.331± 0.001	17.992± 0.016	16.527± 0.005	–	17.393± 0.158	

Continued on the next page